Solar Flare and Coronal Mass Ejection Forecasting Using a Statistically Significant Sample Size of Line-of-Sight Synoptic Magnetograms

A Thesis Submitted in Partial Satisfaction
Of the Requirements for the Degree of
Bachelor of Science in Physics
at the
University of California, Santa Cruz

By
James P. Mason
April 10, 2009

J.Todd Hoeksema
Technical Advisor

David P. Belanger
Supervisor of Senior Theses,
2001-2009

David P. Belanger
Chair, Department of Physics

Table of Contents

ABSTRACT

This investigation uses the entire set of synoptic line-of-site magnetograms from the Solar and Heliospheric Observatory's (SOHO) Michelson Doppler Imager (MDI) to calculate several characteristics of the magnetic field in active regions, including measures of nonpotentiality and field complexity. The magnetic measures are calculated for the disk passage of 1075 NOAA active regions spanning Solar Cycle 23 from 1996 – 2009, which includes 71,324 magnetograms and 12,582 solar flares, in an attempt to determine the ability of line-of-sight magnetograms to be used as a predictor of coronal mass ejections (CMEs) and/or solar flares. Several investigators have analyzed photospheric magnetic field observations to determine the potential for solar flare and CME prediction [Falconer, 2001, 2003, 2008; Leka and Barnes, 2003, 2006; Song, 2006]. Using data from a variety of sources, both line-of-sight and vector magnetograms have been studied. Until now the studies have been restricted to a relatively small sample size.

This expansive study is accomplished by using an IDL code that automatically searches the MDI database for data related to any NOAA AR, uses a three-iteration primary neutral line finder on remapped data [Bokenkamp, 2007], applies a constant-alpha force-free field model [Allisandrakis, 1981], and calculates several measures of nonpotentiality [Falconer, 2008]. Superposed epoch plots were produced for these measures surrounding all X-class, M-class, C-class and weaker flares, as well as active regions that did not flare at all for the entirety of Solar Cycle 23. These plots were used to seek out any pre- or post- flare signatures with the advantage of the capability to resolve weak signals. We find that the gradient weighted primary inversion line length (GWIL) shows promise as a CME/flare predictor.

I: INTRODUCTION

As the closest star to Earth, the sun holds a unique place in astronomy for the study of stellar properties that cannot be ascertained from the specks of light that we receive from more distant stars. Such studies have lead to an understanding of the sun's structure, cycles, electromagnetism and more. It has also been discovered that the sun's behavior is more subtly linked to the biosphere of Earth than may have previously been apparent. In addition to the radiation that is constantly emitted, a stream of solar wind flows outward in all directions. This wind is low-density plasma that breezes through interplanetary (IP) space. The sun occasionally spasms, however, causing a ripple in the solar wind. These events are known as coronal mass ejections (CME). Historically, CMEs have been associated with Solar Flares (SF), which are sudden, intense spikes in the emitted radiation. However, it has been shown that SFs are not necessarily drivers for CMEs (Kahler 1992).

It is generally accepted that both types of events are strongly correlated with complex magnetic field structure and critical energy storage. To date, the difference between the two precise initiation mechanisms is unclear, which is amplified by the fact that more powerful flares are more often associated with CMEs (Schrijiver 2009; Andrews 2003). This suggests that CMEs and SFs are caused by similar, if different, mechanisms (Feynman and Hundhausen 1994; Harrison 1996). Many models exist to explain these mechanisms, with varying degrees of success. Before detailing these models, we will first discuss the observational aspects of solar flares.

In relative terms, solar flares happen very quickly - typically lasting only a few tens of minutes. They can contain anything between 10^{22} and 10^{33} Joules of energy (Zirker 2002 and Fig. 10). There are a couple of different ways that SFs are classified. One method is to describe whether the flare is associated with a CME or not. Eruptive flares (CME associated) emit a full spectrum of x-rays, ultraviolet, and visible light. Confined flares emit primarily hard[1] x-rays. Another method of describing flares is to classify them by their peak flux. The Geostationary

[1] "Hard" x-ray photon energies range from roughly 20 to 200 kev

Operational Environmental Satellites (GOES) continuously measure the amount of radiation in the 100 to 800 picometer range (soft x-ray) emitted from the sun. The team associated with GOES has grouped SFs into five classifications based on their peak flux: A, B, C, M, and X where each letter indicates an order of magnitude increase. The letter classification is supplemented with a numerical linear scale ranging from 1 to 10. For example, this means that an X2 flare would be 20 times more powerful than an M1 flare. Observationally, these events are seen in the first transition of the Balmer spectral series for Hydrogen (Hα), the extreme UV, the radio band, white light[2], and others. In order to understand how flares occur and evolve, many models have been developed. In the present paper, we are primarily interested in initiation of these events; therefore we will focus on the related theory.

The complex magnetic fields described above consist of "flux ropes", which are loops of plasma surrounded by magnetic field that extend through the photosphere[3] i.e. the solar surface into the corona (Fig. 1). The magnetic field in these loops produces pressure that allows the contained plasma to become relatively cool and dense. Incidentally, this is the same mechanism that makes sunspots appear dark (see appendix). If a flux rope appears on the solar disk, it is observed as a dark spot and is labeled a "filament'. If the loop extends from the limb of the sun, it is labeled a "prominence". Either way, they are observed to occur over magnetic neutral lines, which we will define later. The vector magnetic field across the primary neutral line (PNL) tends to be highly sheared, which is indicative of nonpotential energy (Schrijver 2009). There are two competing classes of models for how these flux ropes come into being (Forbes, et al. 2006, and references therein): either they emerge intact through the photosphere or they are formed in the low corona as the result of motion on the photosphere. Figure 1 shows an illustration of one of the simplest models. A loop of magnetic flux emerges from the photosphere and comes into contact with an existing loop of opposite polarity. Magnetic reconnection sets in at what is known as the X-point (green X in Fig. 1). When this occurs, the field snaps into a lower energy configuration. The lowest energy configuration possible is

[2] See glossary for unfamiliar terms

[3] A brief description of the solar structure can be found in the appendix

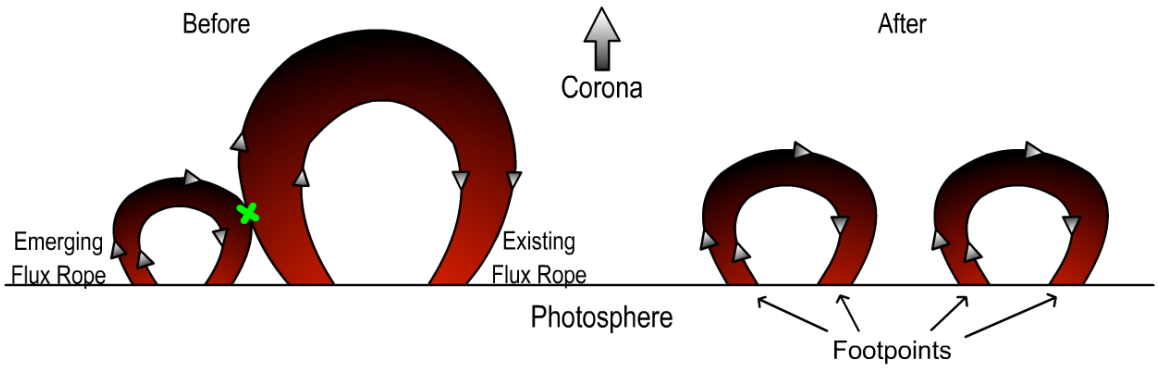

***Figure 1*: Simple flux rope magnetic reconnection model. Flux ropes extend through (not shown) the photosphere into the solar atmosphere. An emerging flux rope comes into contact with an existing rope with opposite polarity. The fields reconfigure into a simpler form and the nonpotential energy is released. The green X represents the magnetic X-point.**

known as the potential force-free field (Sturrock 1991). Any nonpotential energy that is stored in the fields is then released in multiple forms: the surrounding plasma is heated leading to soft x-ray and visible light emission, and ionic particles are accelerated either into IP space or inward to produce hard electromagnetic radiation (Kallenrode 1998). Schrijver (2008), and the references within, detail a more modern and robust theory. In this model, the flux rope takes on a more serpent-like form (see Fig. 2). Next, magnetic reconnection occurs near the solar surface (sometimes referred to as "tether-cutting") through some process similar to that described in the previous model. This enables all or part of the flux rope to break its ties to the solar interior and rise into the overlying corona. Here, the mechanism responsible for differentiating between confined (CME independent) and eruptive (CME associated) flares comes into play. A confined flare will result if the field gradient slows with height or changes sign because the flux rope can become stable again. If the field gradient remains large, then the severed flux loop can proceed into the upper atmosphere and potentially escape as a CME. Note that CME's do not necessarily need to correspond with flaring, although nearly all powerful (X or M class) flares have an associated CME (Andrews 2003; Yashiro et al. 2005; Wang and Zhang 2007).

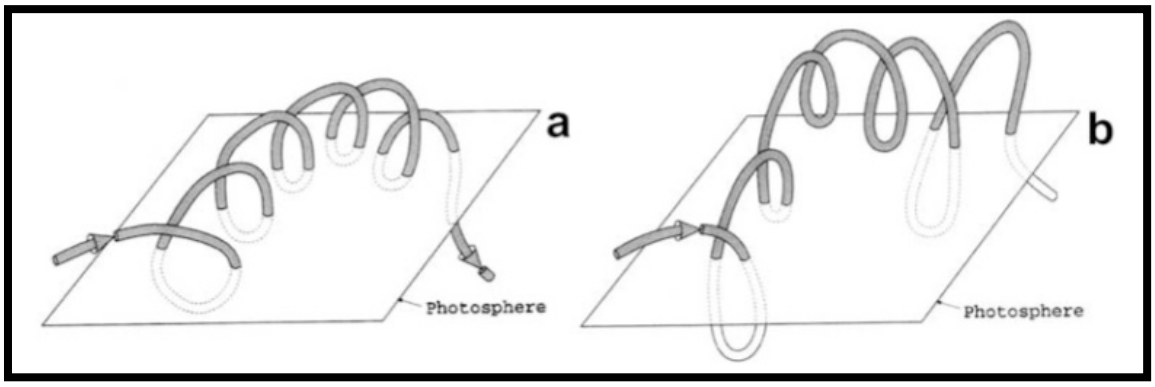

***Figure 2*: Illustration of serpent-like flux ropes. Notice that the single flux rope passes through the photosphere multiple times. Observations of the photosphere would incorrectly assume these to be many separate flux ropes. (Low 2001)**

Since CME's are large masses of ionic particles moving through IP space, their energy is kinetic. The kinetic energy of CMEs ranges from approximately 10^{22} to 10^{24} Joules (Kallenrode 1998). Their speeds range from less than 10 km/s to more than 1000 km/s, which means that the charged particles can reach 1 Astronomical Unit (AU), i.e. the distance from the sun to the earth, in roughly two to five days (Gopalswamy, et al. 2001). Observations of CMEs have served as helpful constraints for theory and models of these events.

In order to eject plasma into IP space, the mass needs to first be present. The flux loops described in the solar flare models serve this purpose and are formed in the same way here. Next, the plasma must be torn from the solar surface and ejected. This requires a destabilization of the flux rope. Apart from the eruptive flare model described above, there are two classes of models for this phenomenon (Forbes, et al. 2006, and references therein): either 1.) the destabilization comes about as a result of footpoint motion, injection of magnetic helicity, or draining of heavy filament/prominence material or 2.) the magnetic structure is already sheared and it becomes unstable due to magnetic reconnection. Here, we will focus on the second model. The magnetic structure is formed by frequent flux cancellations (e.g. magnetic reconnection) of any sheared fields. Since the magnetic field of the flux rope is nearly aligned with the filament/prominence channel, which is often inversely oriented to the polarity of the photosphere, a high shear is natural in this configuration. This means that there is a large nonpotentiality. Continued magnetic

reconnection will increase the magnetic pressure in the rope to a point exceeding the surrounding magnetic tension and lead to an eruption (Fig. 3).

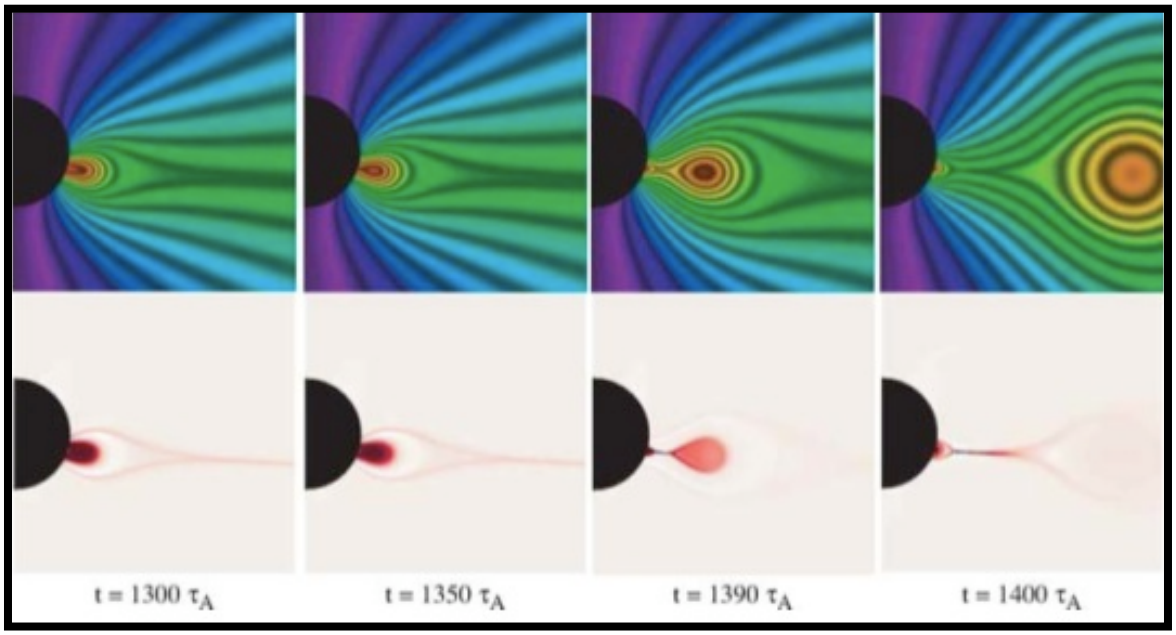

***Figure 3*: Three-dimensional magnetohydrodynamical (MHD) simulation of CME eruption brought on by magnetic reconnection. The top panels indicate the projected magnetic field lines (B_ϕ is perpendicular to the page). The bottom panels indicate the current density. Time is labeled by the Alvén scale time (τ_A = 12 minutes). (Linker, et al. 2003)**

These solar events present interesting physical phenomena to study that are seemingly remote. However, they can have a dramatic effect on the earth through their influence on the atmospheric composition and geomagnetic field. Flares are not capable of magnetic manipulation because they are simply narrow beams of radiation. However, they can influence the temperature and chemistry of the upper atmosphere through ionization. This can cause an increased drag on low-orbit satellites and potentially lead to damage or their destruction if their orbits are not corrected (Kallenrode 1998). Since flares travel at the speed of light, it only takes about 8 minutes for this effect to take place. As previously mentioned, CMEs are composed of charged particles that travel at non-relativistic speeds, but they necessarily interact with any magnetic structure they encounter. If the ejection happens to be oriented toward the earth, the plasma will cause a compression of the earth's sunward magnetic field. This "ram pressure" is strongest if the CME

originates near the solar disk center, has a large southward component of the IP magnetic field, and a large initial velocity (Srivastava and Venkatakrishnan 2004).

Changes in the geomagnetosphere result in a multitude of observable effects. The most common is the aurora borealis/australis, which is the result of the relative gentle breeze of the solar wind. Under normal conditions, the "northern/southern lights" deserve their name, as they are only observable at high latitude. When a CME impacts the earth, the change in the geomagnetic field is much greater. In 1859, a CME impacted the earth with enough ram pressure to create these visible magnetic structures as far south as Boston, Massachusetts (Meriam 1859). While these effects are aesthetically pleasing, there are negative consequences that result from contact with a CME. The powerful alteration of the geomagnetic field can cause massive power blackouts (as in Quebec, Canada 1989), incapacitate satellites (recently a Japanese satellite, Kodoma in 2003), damage long, metallic pipelines, and cause harm to unprotected astronauts. As a result, solar forecasting was developed to attempt predicting these IP storms.

As stated previously, prediction of solar flares and CMEs depend on two things: magnetic field complexity and critical energy storage. A useful analogy is to compare the magnetic field lines to rubber bands. When one twists, torques, and stretches a rubber band, two things occur: the rubber band's configuration becomes more complex, and energy is stored in it. If too much energy is stored, the rubber band snaps, leaving the system in a lower energy configuration. Combining this rubber band with dozens of others causes the situation to become much more complicated. Thus, the difficulty in predicting "snap" events comes from quantizing the concept of nonpotentiality (i.e. energy stored in nonpotential fields). The regions of the most magnetic complexity on the sun are labeled Active Regions (AR), which underlie sunspots. Hence, these are the primary regions of interest for measuring nonpotentiality, as the majority of high-energy events come from these locations. There is a horde of measures for nonpotentiality that have had various degrees of predictive success.

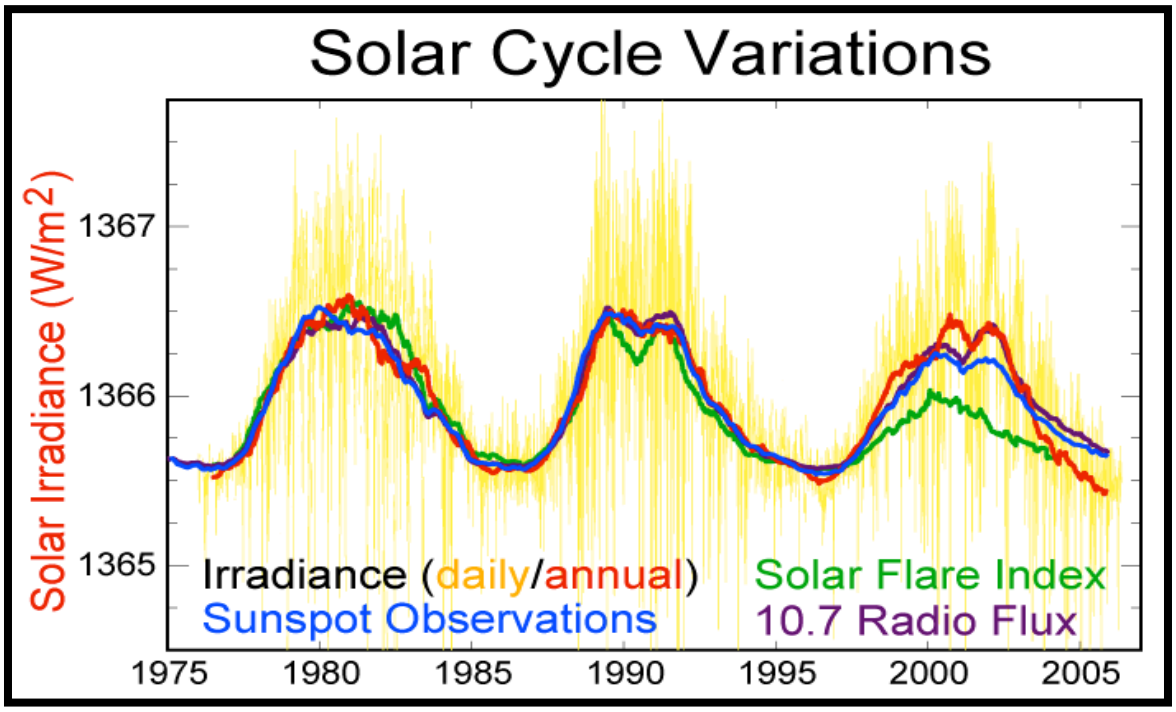

***Figure 4*: Plot of several solar parameters that are shown to vary with the 11-year solar cycle. "10.7" refers to the 10.7 centimeter band of the radio spectrum. Particularly pertinent to this paper is the solar flare index. (Rohde 2008)**

Prediction of these events has only become feasible in recent decades. In 1966, Patrick McIntosh introduced a qualitative sunspot classification scheme that became widely used in the space weather communities (McIntosh 1990). Another intuitive method of forecasting is to use the well-established eleven-year solar cycle. A large number of processes related to solar activity vary with this cycle (Fig. 4). The magnetic structures that compose active regions and that are responsible for sunspots are one such process. Figure 5 illustrates this with a plot of the area of sunspots from the last 140 years.

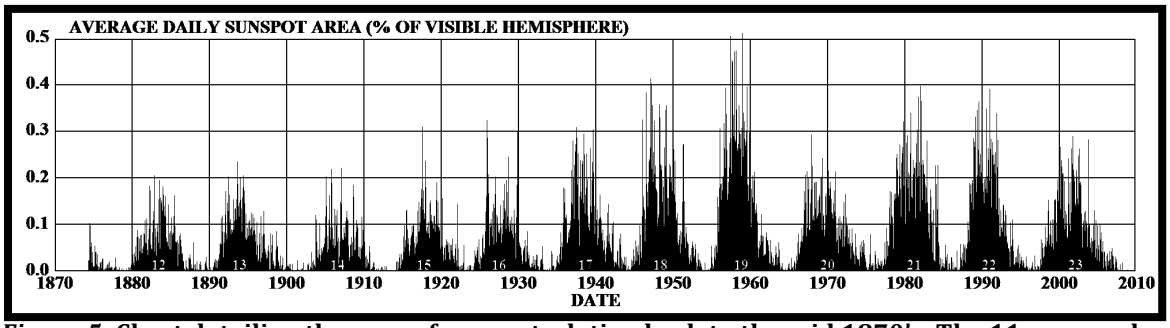

***Figure 5*: Chart detailing the area of sunspots dating back to the mid 1870's. The 11-year cycle is apparent here. During solar maximum (most recently ~2000-2003), the area of sunspots drastically increases. (D. Hathaway 2009)**

It can be inferred from this graph that there is more magnetic complexity during the solar maxima, and therefore more frequent energetic events. Referring back to Figure 4 shows that this is in fact true[4]. During solar maximum, roughly two or three CMEs are observed per day but during solar minimum there is only about one per week (D. H. Hathaway 2007). However, these are not quantitative methods for prediction or forecasting; they only give a general sense of when CMEs/SFs may occur. Many researchers have attempted to develop this quantitative predictor. Guo and Zhang (2006) tested a potential measure of nonpotentiality deemed the "effective distance". This quantity is the distance between the flux-weighted centers of the bipolar region constituting the AR (further detailed in Data Analysis). They found that this quantity correlated well with flaring intensity. Falconer et al. (2001) tested the correlation between AR CME productivity and several possible measures of nonpotentiality such as the length of the strong-shear, strong-field main neutral line (see Data Analysis). Falconer et al. (2003) then generalized the aforementioned measure, which will also be described in detail in the analysis section. Song et al. (2006) found that the angle between the projected field lines over the magnetic neutral line and the southward direction is a good predictor of super-storms. However, there are researchers who are more skeptical of the possibility of only using magnetic data to predict CMEs and SFs. Leka and Barnes (2006) found that the magnetic field at the photosphere is only moderately related to the flare productivity of the region. Barnes and Leka (2008) show that the best measures of magnetic nonpotentiality are as good at forecasting flares as independent methods, and suggest that forecasting may be improved by combining these methods. The above papers were either limited by a small sample size or were focussed primarily on soemthing related to, but not exactly, CME/SF prediction. The present paper expands these earlier studies to a statistically significant sample using the entire history of Michelson Doppler Imager (MDI) synoptic line-of-sight magnetograms. This paper also describes the automated tool that has been developed for calculating various parameters from said magnetograms.

[4] Note that this may not necessarily be true for large/powerful flares (see Hudson 2007)

II: DATA AND METHOD

II.1: INITIAL DATA COLLECTION AND EXTRACTION

The data used for this study come from an instrument onboard the Solar and Heliospheric Observatory (SOHO). This satellite orbits the earth-sun L1 Lagrangian point, which gives it a full-time unobstructed view of the sun. The 12 instruments onboard take a variety of measurements, but here we are primarily concerned with the photospheric magnetic images taken by the Michelson Doppler Imager. This instrument measures the line-of-sight magnetic field of the entire solar disk at the relatively high resolution of ~2 arc seconds per pixel (see an example in Fig. 6). MDI produces full disk line-of-sight magnetograms at a cadence of 96 minutes, with a temporal resolution of 30 seconds. There is about 20 Gauss of noise in the field density per pixel (Scherrer, et al. 1995). If noise reduction is desired, MDI can average five 30-second magnetograms to achieve a noise level of approximately 9 Gauss. These products are available from 1996 to the present date, and they continue to be produced. This study uses the recently recalibrated level 1.8 synoptic line-of-sight magnetograms. MDI images the sun as a flat disk. However, the sun is, in reality, three-dimensional object. This discrepancy causes a distortion in the measured magnetic field, which is accounted for by Bokenkamp (2007)[5].

The present paper includes the analysis of 1075 active regions visible in the MDI magnetograms that span from April 15, 1996 to December 31, 2008[6]. ARs on the backside of the sun could obviously not be observed. In addition to this loss of potential data, other selection criteria were applied to the larger dataset.

In order to be included in this study, ARs had to be sufficiently large[7] because very small ARs decay very quickly and very rarely produce any energetic events. Second, MDI data of the AR needed to be available within 30 degrees of disk center. This reduces the amount of projection error due to the discrepancy between the real

[5] Bokenkamp provided many of the basic program routines used in this study.

[6] Currently, the sun is extremely quiet with very few sunspots/ARs.

[7] Hα sunspot size of AR greater than 1/10,000 of visible solar hemisphere, as estimated in the NOAA database

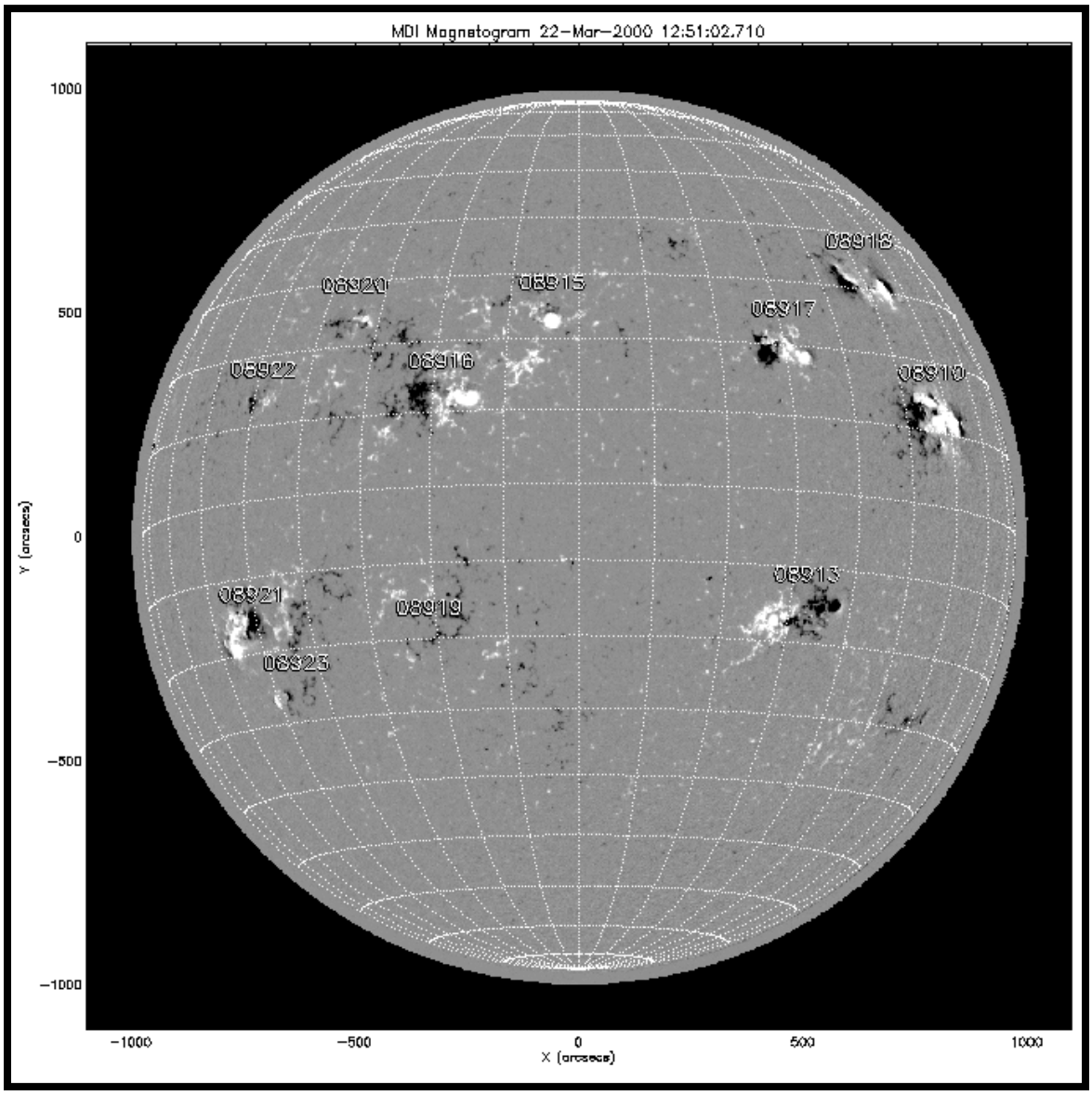

***Figure 6*: Example of a full disk Michelson Doppler Imager (MDI) line-of-sight magnetogram taken March 22, 2000 at 12:51 PM UT time. Black and white coloration indicate negative and positive flux, respectively. A latitude-longitude grid has been overlaid. The National Oceanic and Atmospheric Administration's (NOAA) active region (AR) numbers have been labeled. Note AR 8910, as it will be used as an example later in the text. (Gurman 2000)**

spheroid and the image disk, as described above. Finally, bad images were removed. Bokenkamp (2007) did this manually by watching movies of his 1037 ARs as they evolved across the solar disk. This method has been improved by using the Quality Bits included as a keyword in all the magnetogram data. A mask string was created to screen out the bad data: "0x402c0c04". This string removes data that has been labeled "bad" for obscure reasons, that contains data statistics problems, stored

magnetogram corruption, excessive cosmic ray hits, onboard processing errors, missing observation time, or any amount of the image missing. The last of these is the only one that Bokenkamp (2007) could have confirmed visually, leaving other bad data to skew later calculations.

Other improvements have been made on the original Bokenkamp (2007) program. Figure 7 outlines the entire automated procedure. The program can now run on any computer system[8] that has access to the solar software suite that is distributed for the SOHO science teams. It can also now accept any number or range of specific National Oceanic and Atmospheric Administration (NOAA) ARs or dates. This is a significant improvement on the original program that required the input of a single NOAA AR number at a time, considering there are over one thousand such numbers. The program uses the NOAA daily solar regions summary, which contains the AR number, location, type and approximate size. The location data is used to find the full-disk magnetograms that contain the specified AR because the MDI data does not include these labels. Next, sub-images were extracted from the full-disk magnetograms that corresponded to the size and location of the AR as indicated by the NOAA catalogue. A buffer area was included around NOAA's approximate size to ensure that all elements of the active region were included for analysis. The addition of this buffer scales with the size of the AR itself. The Solar Oscillation Investigation group's strategy module project was used to do the actual extraction of sub-images while flattening the image using an equidistant azimuthal projection. This method yields better estimates of distance on the solar surface, which will be applied later in the Data Analysis section. Figure 8 shows an example of one of these sub-images. Once the sub-image extraction is complete, we can run calculations on the active region.

[8] Requires a 32 bit processor to create movies of AR evolution

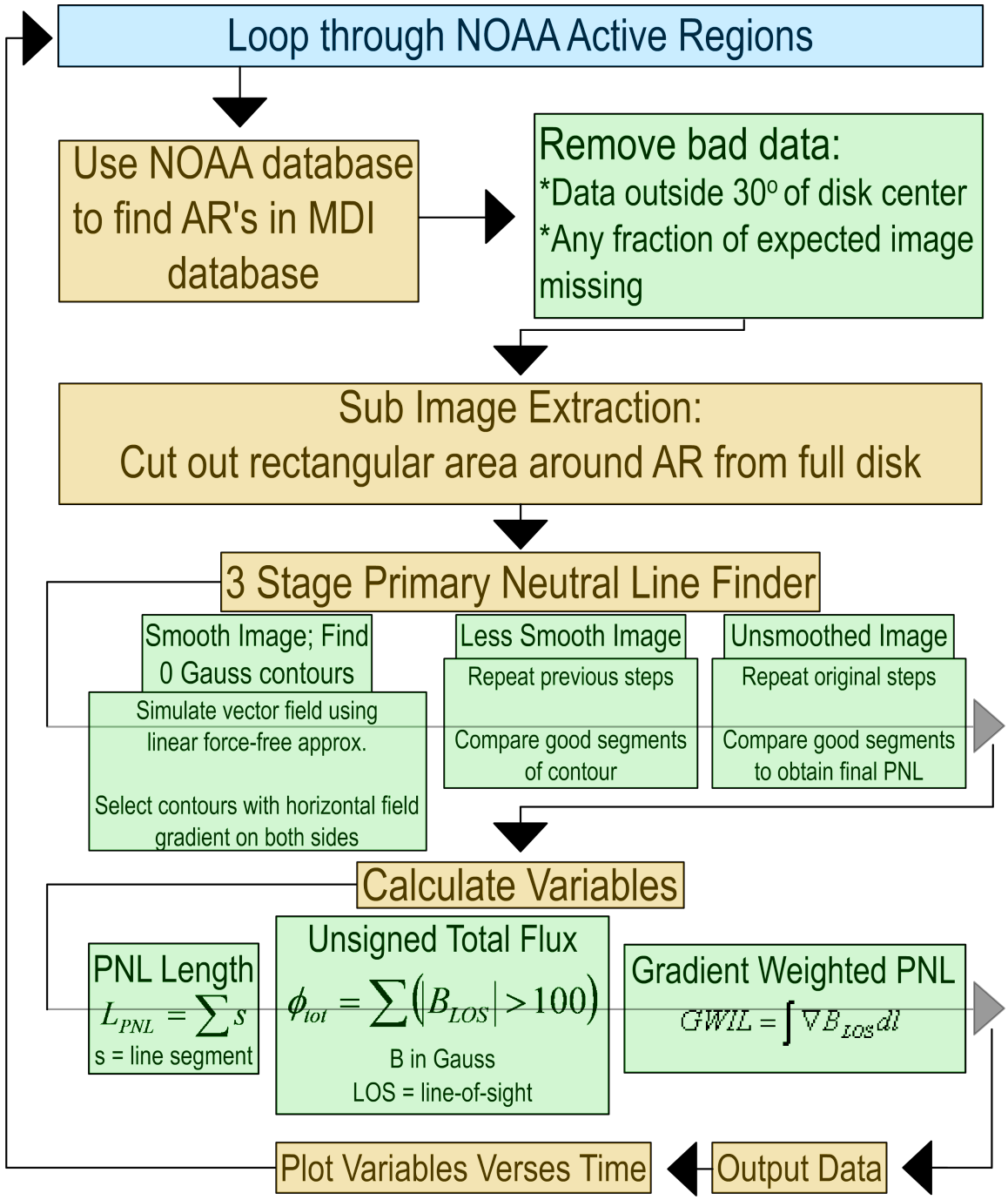

***Figure 7*: Flow chart outline of the procedural program used to generate the parameters described below. Effective distance and the gradient across the neutral line are not included in "Calculate Variables" in the interest of simplification. A large amount of work went into streamlining and generalizing this code.**

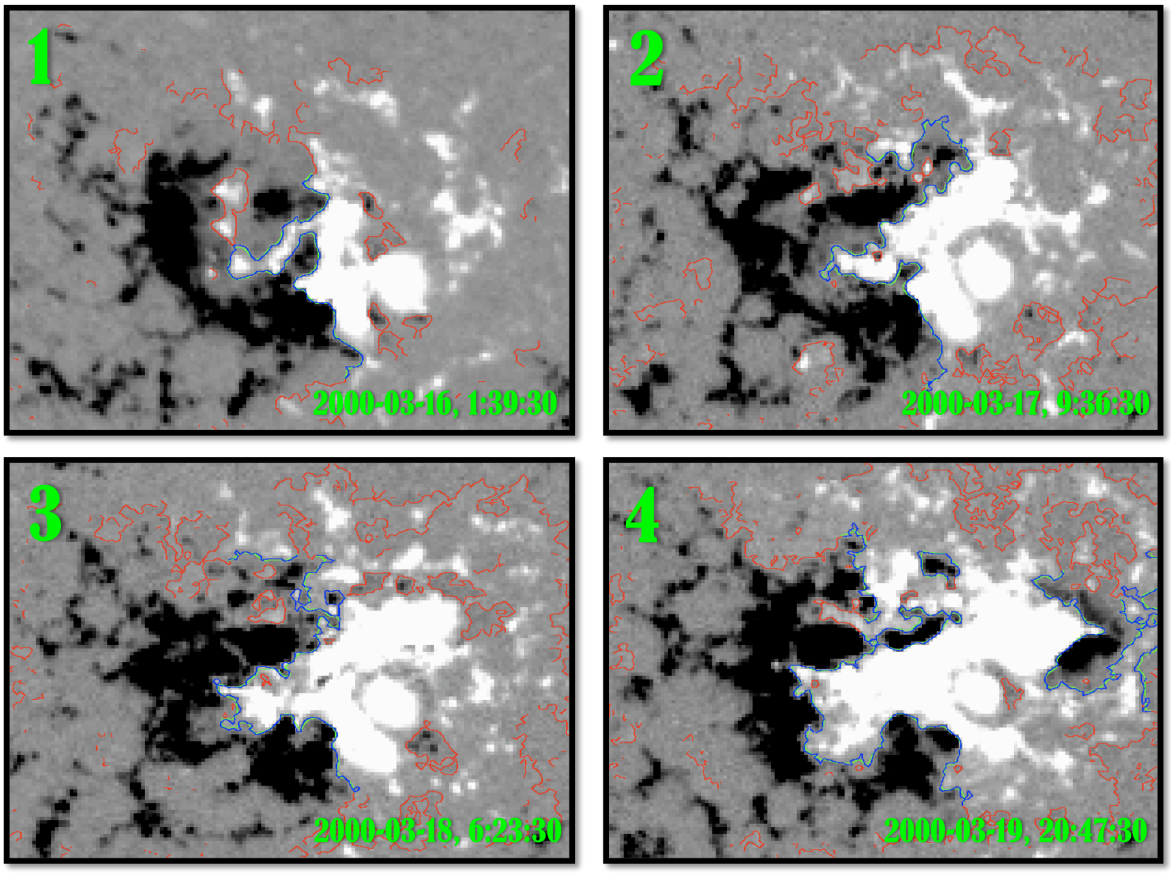

***Figure 8*: Sub-image extraction of NOAA AR 8910 at four different times to illustrate active region evolution. Note that all images are within 30° of disk center. Red lines indicate the program's first attempt to trace the Primary Neutral Line (PNL). Blue line indicates 2nd attempt, using a smoothed image, and green line represents final P_{NL} calculation. Also note the black and white (i.e. negative and positive flux) bipolar regions.**

II.2: Calculated Variables

In this section, the variables we chose to measure as representing the nonpotentiality and/or magnetic complexity of the active regions are detailed. In the Data Analysis section, the justification for each of these variables being such a measure is provided, as well as publications to support the claim.

Unsigned Total Magnetic Flux

As previously mentioned, ARs with larger area cause the buffer area around them to be larger as well. This effect causes a skew in the calculation of the total flux, tending to amplify the value for regions that are already larger (Bokenkamp 2007). Measurements of the magnetic field in the umbrae of sunspots (i.e. densest region of

ARs) sometimes become saturated (Liu, Norton and Scherrer 2007), which tends to skew the total flux value downward. These competing effects are nontrivial to correct, so we caution the future results of this variable. We apply a threshold of 100 Gauss in our calculation in order to reduce the effect of noise:

$$\phi_{tot} = \sum_{i}^{N} \left(|B_{LOS}| > 100 \right) \tag{1}$$

where B is measured in Gauss, LOS stands for line-of-sight, and N is the total number of pixels in the sub-image.

Primary Neutral Line Length

Neutral (or inversion) lines are the barriers between patches of positive and negative flux. These occur all over the sun, and are particularly numerous in the area surrounding an active region. The primary neutral line (PNL) separates the major bipolar regions of an AR (see Fig. 8). This line is very easy to trace by eye, but it is more difficult for a computer to do so properly. Bokenkamp (2007) developed an IDL program to effectively find the PNL using a 3-iteration process. First, the sub-image is strongly smoothed and contour mapped to find the 0 Gauss contours. Smoothing is an effective method of removing the small-scale structures that generate neutral lines that are off the PNL (see red lines in Fig. 8). A vector field is then simulated using an alpha=0 force-free potential model (Alissandrakis 1981) in the same method as (Falconer, Moore and Gary 2001). This stage selects contours with horizontal field gradient on both sides above a specified threshold and with a strong simulated vector magnetic field strength. Second, this process is repeated for a less smoothed image. The good segments of this stage are compared with the previous. Finally, the same process is applied to a completely unsmoothed image and the segment comparison results in a fairly accurate representation of the PNL. The length of this line is calculated using the equation

$$L_{PNL} = \sum_{i}^{N} s \tag{2}$$

where s is the individual line segment, and N is the total number of line segments. The average gradient of the magnetic field across the calculated PNL is also calculated.

Effective Distance

This measure was first proposed by Chumak and Chumak (1987). Geometrically, it is the distance between the two bipolar regions of an AR (see Figure 8). First, the two regions are weighted by the amount of flux they contain and the centers are found. Then the distance between the centers is calculated. This distance is indicative of how smashed together or isolated the bipoles are (Guo and Zhang 2006). Large values indicate a fairly well separated AR, while smaller values indicate a densely packed active region.

Gradient Weighted Inversion Line (GWIL)

The length of the gradient weighted inversion line (herein refered to as GWIL) corresponds closely to the parameter L_{SG} that Falconer (2003) proposed, which will be detailed in the Data Analysis section. This parameter is calculated by applying the equation

$$GWIL = \int \nabla B_{LOS} dl \tag{3}$$

where the integral runs along the entire length of the PNL. This measure tends to emphasize regions of the AR that are strongly sheared and magnetically complex.

II.3: PROGRAM OUTPUTS

In order to determine a relationship between the variables calculated and the AR's energetic event productivity, the associated events must first be catalogued. GOES monitor the near earth x-ray flux and have been doing so for longer than the SOHO has been in operation. Therefore, this catalogue is a consistent database for all solar flares occurring within our large data sample. Each flare has been associated with an AR through their observed locations in Hα images (Bokenkamp 2007). Flares that are unassociated with any specific AR were not included in our analysis. For every AR, a time series plot was created for each calculated variable with the temporal location of any M class or stronger flares indicated (see an example in Fig. 11).

The data output for every magnetogram included in this study were placed in a single table and made available to the public[9]. There are 71,324 magnetograms included in our "Great Table", each with their corresponding NOAA AR number, date, time, MDI fits file identifier, Carrington location, pixel size of sub-image, and the five calculated variables. The flare table with the date, start time, end time, time of maximum flux, solar location, GOES classification, and associated NOAA AR number of each of the 12,582 flares is also publically available[10].

III: DATA ANALYSIS AND RESULTS

Given the enormous table containing measures related to the photospheric magnetic field that we discussed in the Data and Method section, the first natural question to ask is what the entirety of solar cycle 23[11] looked like. An effective way to view this large amount of data is with a histogram. We have generated histograms for all of the parameters described in Data and Method, but only include the unsigned total flux, effective distance, and GWIL in this paper because the PNL length and gradient across the PNL are both effectively included in GWIL (Figure 9). For each specific parameter, we took the maximum value in each AR and counted how many ARs had that value. We separated the solar cycle into its minimum, maximum, and declining phase, as detailed on the graphs.

It can be seen in Figure 9-A (GWIL histogram) that the number of ARs with a specific value of GWIL is inversely proportional to the value itself. Low values of GWIL are indicative of a small, simply-configured AR whereas large values of GWIL indicate a large, magnetically complex AR. Therefore, the histogram's trend makes sense because lower energy processes tend to occur more frequently in all aspects of nature (also see Figure 10 for a similar scenario). Note that the extremely small values of GWIL do not follow this general trend. This is due to the bin size selected for the histograms. Values of this size are difficult to obtain because they barely

[9] http://soi.stanford.edu/~jmason86/GreatTable
[10] http://soi.stanford.edu/~jmason86/FlareTable
[11] Solar cycles have been traditionally labeled by number ever since Rudolf Wolf defined solar cycle 1, spanning 1755-1766.

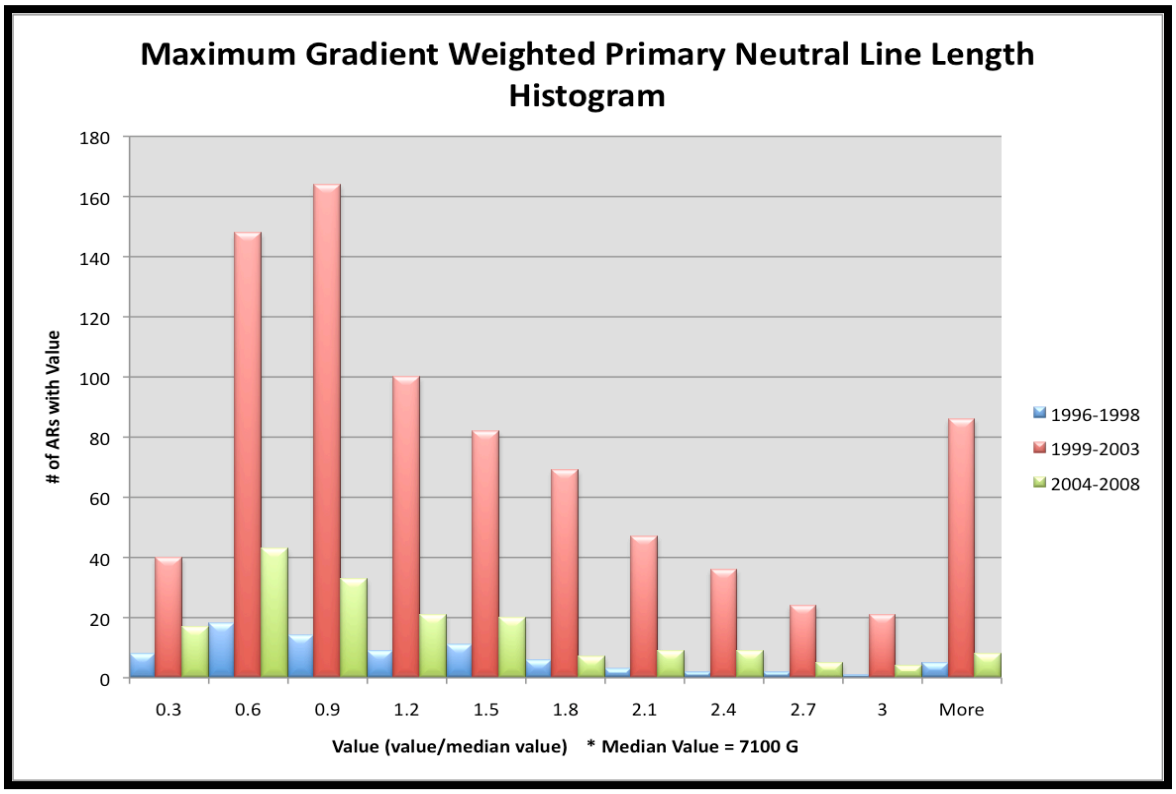

***Figure 9-A*: Histogram of maximum value of GWIL of each AR. The blue, red, and green series roughly represent the solar minimum, maximum, and declining phase, respectively.**

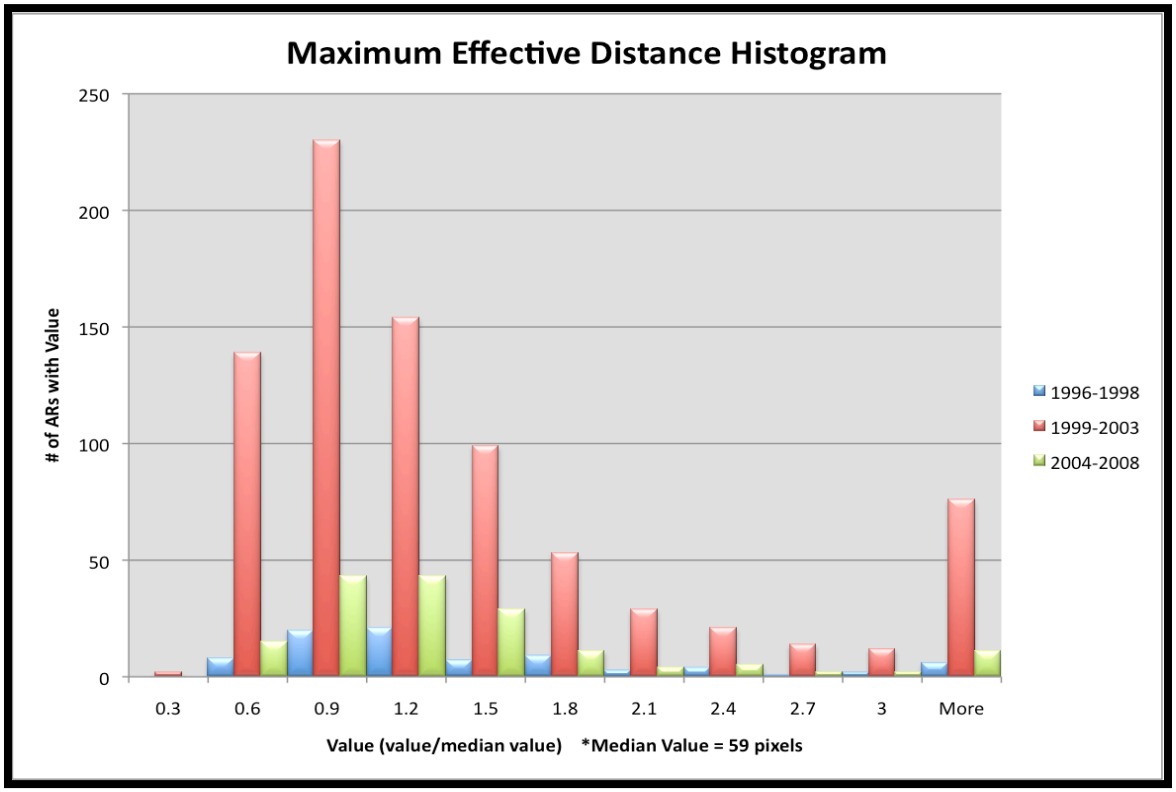

***Figure 9-B*: Histogram of maximum value of effective distance of each AR. Same color-coding.**

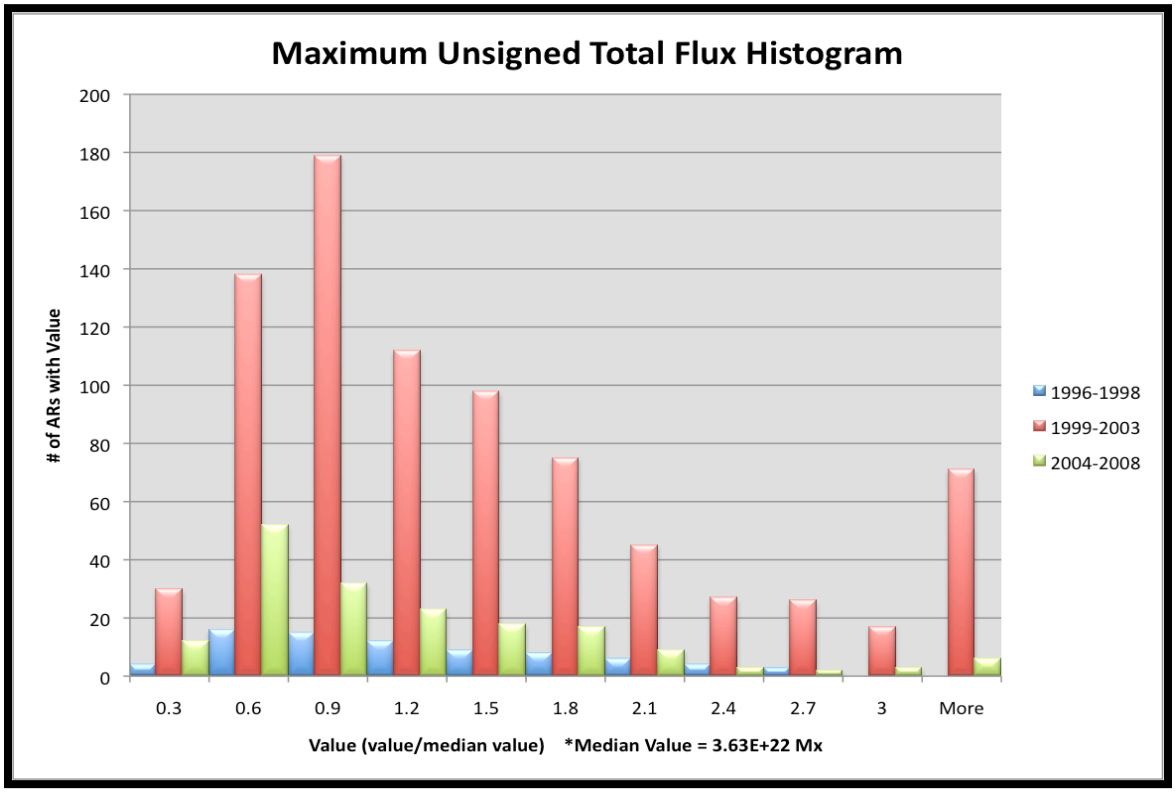

***Figure 9-C*: Histogram of maximum value of unsigned total flux of each AR. Same color-coding.**

constitute an AR at all; they only just stick out of the constant bubbling froth of the solar surface. This histogram also shows that the number of active regions with *any* value is the highest during solar maximum. This time period is particularly dominant in the far-right tail of the distribution. Here, the difference between solar maximum and the minimum/declining phase is most obvious. This relates to our comment in the Introduction that there are many more energetic events occurring during the solar maximum. We expect that the largest values of GWIL will come from ARs that also happen to flare. Therefore, this is a promising, but not altogether convincing, result. The effective distance and unsigned total flux (Fig. 9-B and C) show the same trends. The latter shows a noticeable fluctuation in the solar minimum. Note that there are less than 20 ARs in each bin, which makes this time-period more susceptible to statistical fluctuation. The total flux during solar minimum is particularly sensitive to perturbations; single events can have a large impact on the overall total flux because the majority of the sun is very quiet.

The parameters we chose to calculate were based on their predictive success in previous studies. Bokenkamp (2007) found that the length of the PNL was well correlated with an ARs overall flare productivity. He found that regions with values between 400 and 500 had an 80% likelihood of being flare productive, and regions with values greater than 500 had a 90% chance of flaring over their lifetime. He also found that there was no *temporal* correlation between this parameter and flare productivity i.e. it could not be used to predict a flare prior to its occurrence, only to predict an ARs propensity to flare. Conceptually, a longer PNL indicates a more complex magnetic field structure. The simplest case would be an AR where the two bipoles only touch at one point. This would mean that the regions are fairly well separated and the inward and outward flux are not intermingling very much. However, it does not take into account the size of each bipolar region or the difference in the absolute value of the flux on either side.

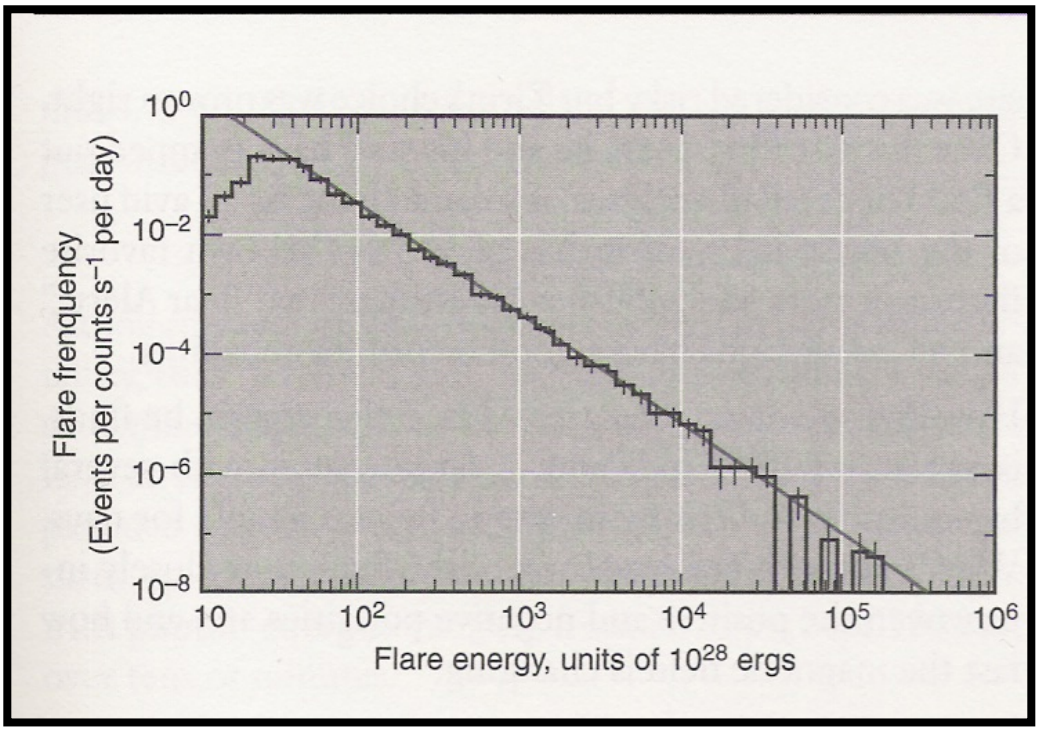

***Figure 10*: Logarithmic plot of flare energy versus frequency of occurrence. Note that weak flares are much more common than strong ones. (Zirker 2002)**

Bokenkamp (2007) also tested the gradient across the PNL. He found this parameter to have some potential for prediction 0-12 hours prior to flaring. This parameter also shows promise for use as an automated image recognition system

for ARs in line-of-sight magnetograms (Song, et al. 2006). If such a technique[12] could be perfected, it would eliminate the dependence on NOAA active region identification and result in very near real-time solar forecasting. A large gradient indicates an appreciable difference in the magnetic field over a relatively small distance. This is indicative of shearing or twisting of the magnetic fields. As described by the rubber-band example, shears and twists are methods of storing nonpotential energy.

Chumak, Zhang and Guo (2004) and Guo (2006) found the effective distance to be a useful parameter for flare prediction. As stated in the Data and Method section, small values of effective distance are indicative of a dense active region. Such regions are likely to contain a lot of intermingling flux, which is also likely to cause large gradients, potentially even off the PNL.

Falconer and Moore (2003) showed that L_{SG}, the segment of the PNL that has a gradient above 50 Gauss per megameter, is a line-of-sight magnetogram derivable proxy for the vector-derived quantity, L_{SS}, the strong shear length. L_{SG} uses simulated transverse fields (as our GWIL does) in place of the observed vector field used for L_{SS}. Where Falconer and Moore (2003) cut off the length of the PNL with the gradient below their threshold, we simply weight these segments less. The resultant quantity should be a better measure for nonpotentiality than the standard PNL used in Bokenkamp (2007). The advantage of GWIL is that it benefits from the best of both the PNL and the gradient across it; GWIL is larger for ARs that have long PNLs that are indicative of a complex field structure, and is also larger for high gradients, which is indicative of shearing and nonpotentiality.

To date, many of the studies that have been performed have been limited to relatively small sample sizes. Large sample sizes are extremely important in this area of research because we are primarily interested in the rarest events: those that contain a large amount of energy and present a serious threat. Since 1996, there have only been approximately 100 X-class and 373 M-Class front-side solar flares. During the same time period, the weaker B and C class flares have occurred 1000

[12] Peter Schuck at the U.S. Naval Research Laboratory is currently developing an independent method of AR identification.

times (in regions that lacked more powerful flares). We label these "quiet" regions. Finally, of the 1075 ARs studied, 418 of them lacked any sort of flaring whatsoever. We label these "Dead-Silent" regions. This trend of peak intensity versus frequency of occurrence can be seen in Figure 10. Since powerful flares do not occur very often, it is necessary to study as large a time period as possible to obtain results of statistical significance. With our 1075 ARs, we still only find ~100 X-flares which means that we cannot divide them into too many sub-categories without affecting the statistical validity of our results. In the limit, we would study each X-flare associated AR individually. The individual plots produced by the program outlined in Figure 7 can be studied, but any results derived from them may be misleading. Figure 11 displays three examples of individual plots.

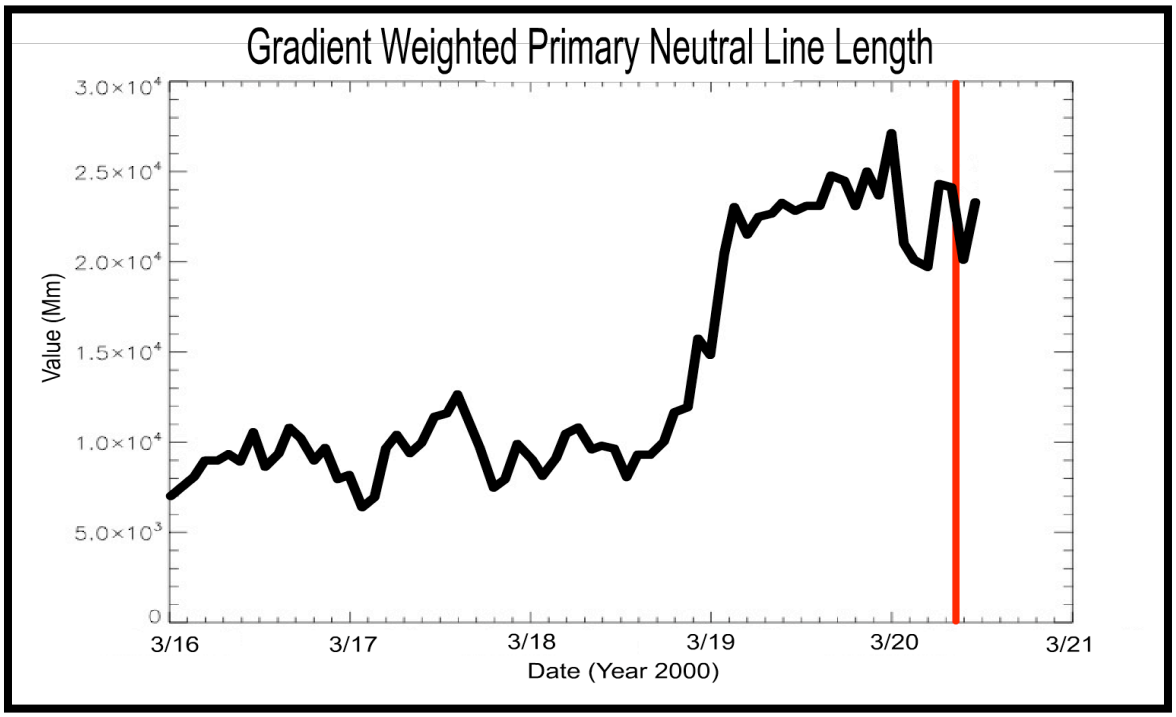

***Figure 11-A*: Evolution of GWIL for AR 8910. Red bar indicates time of M2.4 flare. Note the drastic increase approximately 1.5 days prior to flaring.**

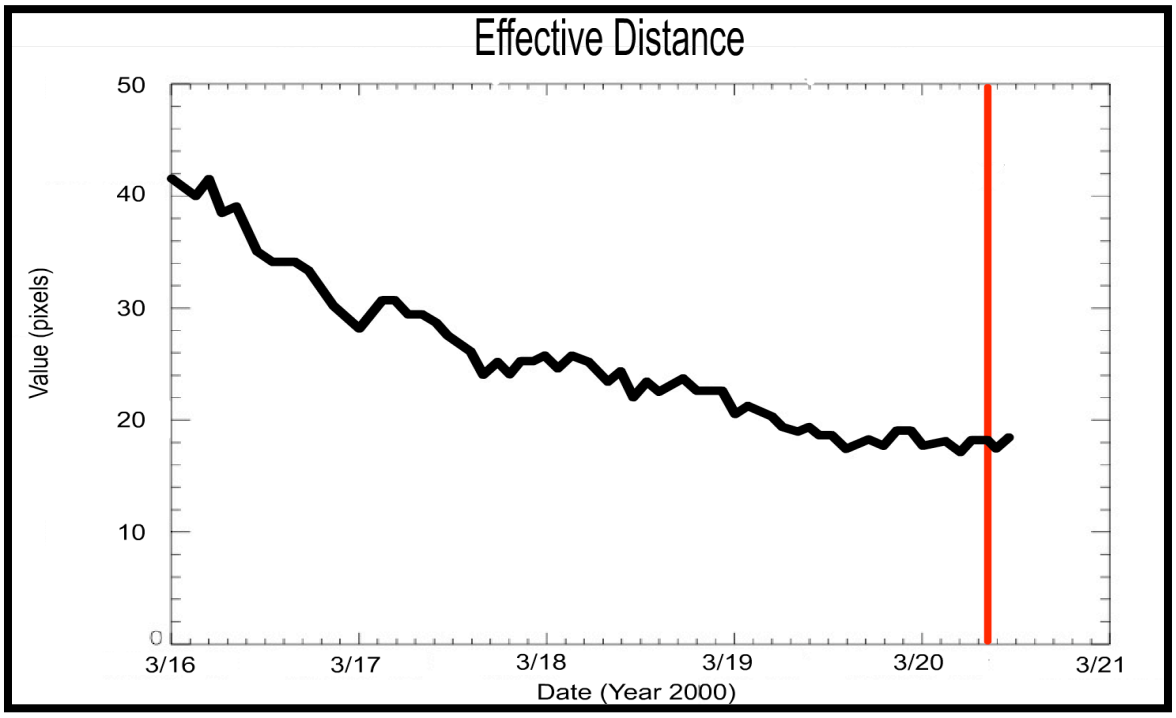

Figure 11-B: **Evolution of the distance between flux-weighted centers of the ARs bipolar regions for AR 8910. Red bar indicates time of M2.4 flare. Note a general decrease over the AR disk passage and a plateau roughly 1 day prior to flaring.**

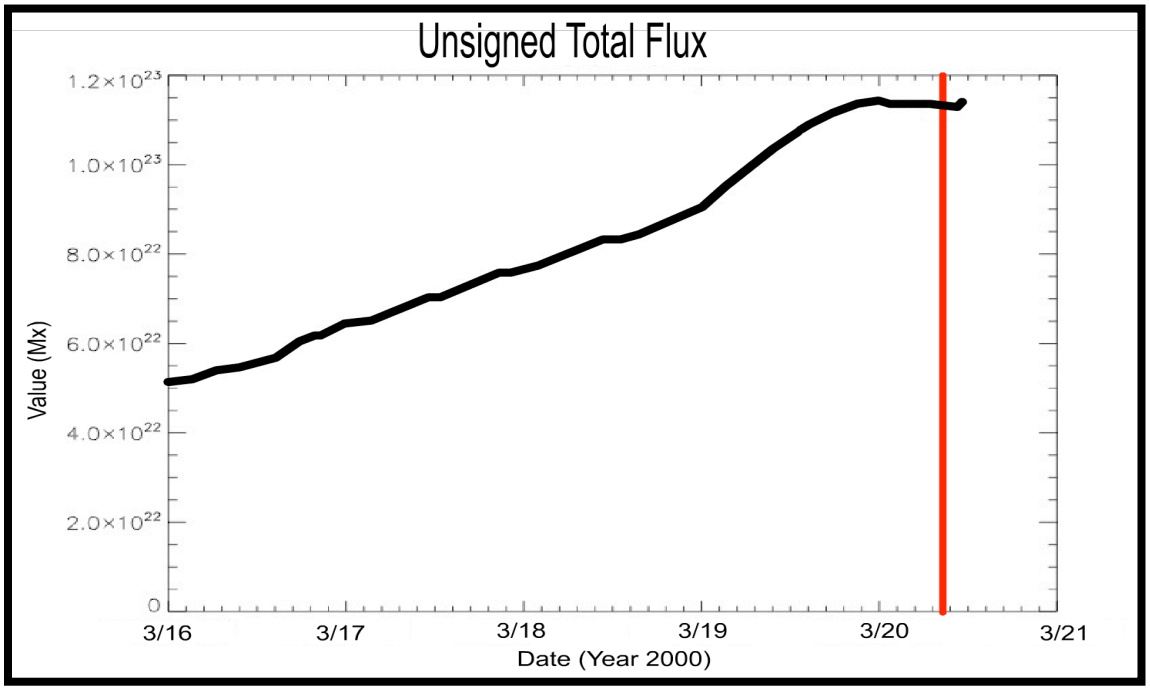

Figure 11-C: **Evolution of unsigned total flux for AR 8910. Red bar indicates time of M2.4 flare. Note the general increase over the AR disk passage and a plateau a few hours prior to flaring.**

For NOAA AR 8910, all three of the displayed variables seem to have a significant reaction to the labeled M2.4 flare. If the variables behaved like this every time there was an imminent flare, there would be little work left in solar forecasting. Researches tend to study the most interesting events, which usually look something like the above plots. Then they make a conclusion about the predictive success of their parameters based on only a few examples. We would like to test the general case by combining as many of these plots as we can.

Superposed Epoch (SPE) plots are a convenient way of viewing a large number of data series over a period of time. Essentially, our SPE plots are the combination of multiple individual plots with the temporal location of the flare aligned in each. We can align to any time, whether or not it corresponds to a flare, with what we label a Keytime. Our analysis code accepts a list of Keytimes, or a Keylist, and finds the data, if any, from our Great Table. For any specific nonpotentiality measure, we align the data so that the Keytimes are set to t=0 for every data series. Since MDI takes magnetograms at a 96-minute cadence, our data series exist as a succession of points 96 minutes apart. The Keytimes are independent of this grid, so when we justify multiple series to the same point, the data points will not necessarily line up. To prevent this from become a problem, we alter the Keytime slightly to match the nearest grid point in its data series. We created a separate Keylist for the X-class, M-class, and quiet flares, as well as the Dead Silent regions (see above). If multiple flares occurred in a single AR, the Keytime was chosen to represent the temporally central flare. For Dead-Silent regions, we chose the Keytime to be near the ARs central meridian passage time. While overlaying the plots in the manner just described is useful for identifying potential outliers, it can become very jumbled, particularly for the quiet regions where there are 1000 lines to superpose. A more useful method is to combine them in a meaningful way. We calculated the first four statistical moments of each point along the grid to produce a more coherent picture. Both of our primary parameters (GWIL and effective distance) have a plot for the mean, variance, skewness, and kurtosis for each of the four Keylists.

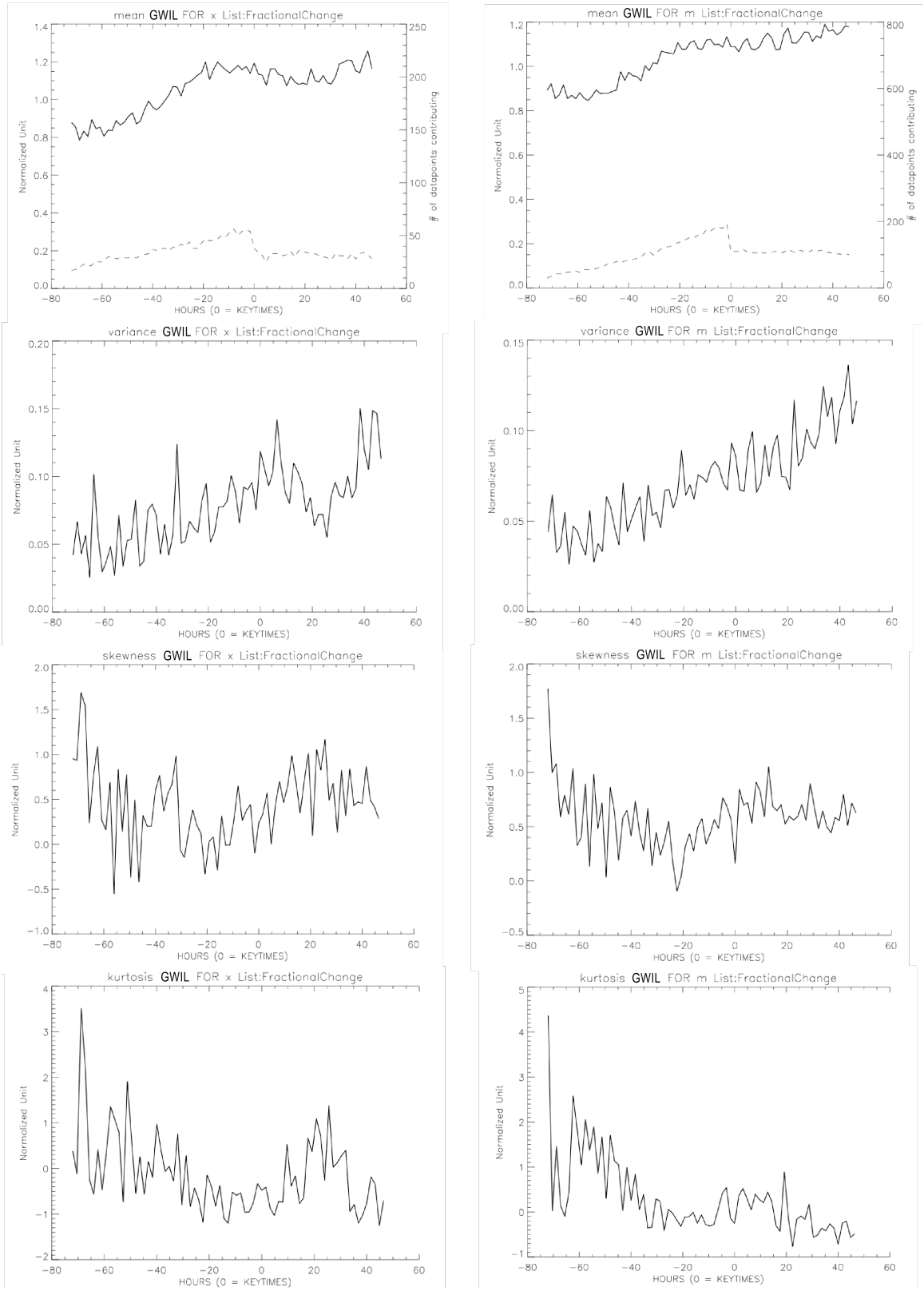

***Figure 12–A*: SPE plots of GWIL for the X- (left column) and M- (right column) flare Keylists. The first four statistical moments of the distribution are plotted: mean (row 1), variance (row 2), skewness (row 3) and kurtosis (row 4). Units are normalized by average.**

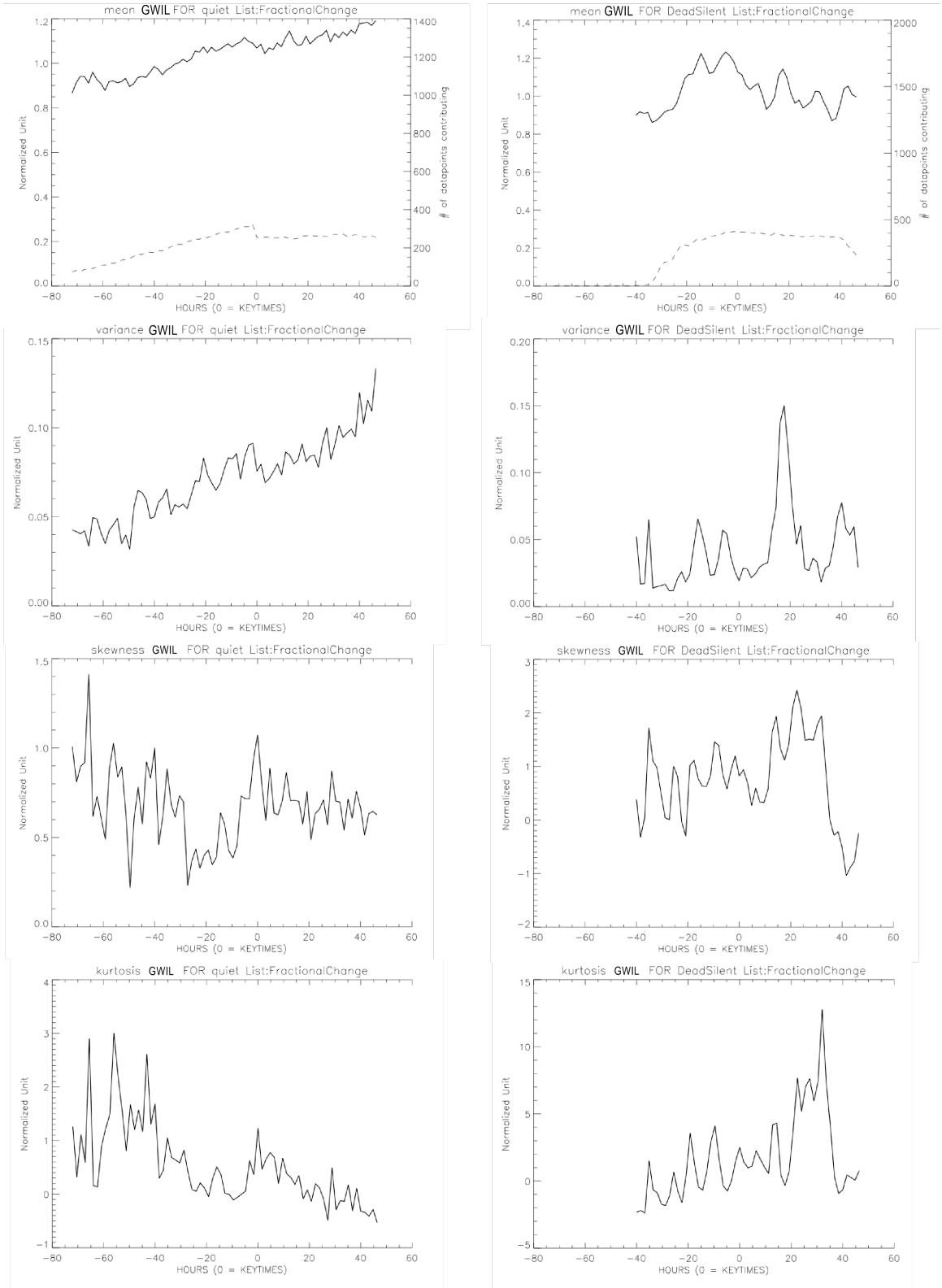

***Figure 12-B*: SPE plots of GWIL for the Quiet–flare (left column) and Dead-Silent region (right column) Keylists. The statistical moments and units are the same as in Figure 12-A. The dashed line indicates the number of points contributing to the mean and all other statistical measures but is only shown on the mean plots to avoid redundancy (scale on right axis).**

All of the above plots have been normalized by dividing each series by their average value before combining them in the SPE plotting procedure. Our goal is to see what *tends* to happen at each point in time prior to (or after) a flare. We include the Dead-Silent regions as a control.

One can imagine a 3-D superposed epoch plot, where the x-y axes are the same as those above, but each data series is plotted a fixed distance apart in the z axis. Then one could rotate the graph to view the z-y plane for any given x (which would still be a fixed 96 minute grid). We would like to know what the distribution in the z-y plane looks like. The statistical moments of the distribution are a way of describing this. To completely describe any distribution, an infinite number of moments would be required but the first four are commonly used because they provide a fairly accurate picture. The mean[13] describes the central location of the data. This gives us a sense of what the typical value is. However, if there are a few enormously large or small values (outliers i.e. not what *typically* happen) then the mean will be thrown off. The variance is a measure of the distribution's dispersion. Small values indicate the data are clustered tightly around the mean, whereas large values indicate that distribution is spread out. It is possible that most of the data are on the more powerful side of the mean. This would be an asymmetrical distribution and would result in a negative skewness. Skewness is positive for values that have a longer right-side tail, which implies that most of the "mass" of the distribution is on the left i.e. the y-axis variables tend to be smaller than the mean. The fourth statistical moment is the kurtosis, which measures how peaked the distribution is. Negative values indicate that the distribution is more square with a flatter top and positive values indicate a stronger peak, where a value of 0 is reserved for Gaussian distributions. Also, higher values of kurtosis imply that more of the variance comes from only a few outliers, whereas low values suggest that the variance is primarily due to frequent moderate deviations.

[13] The mean and variance can be undefined for distributions that do not have a tendency to cluster around some central point (Numerical Recipes 3rd Edition 2007)

At this time, we have not developed a quantitative means of analyzing these plots. However, based on the knowledge of the statistical moments just described, we can derive some tentative conclusions. The mean value of the gradient weighted neutral line length (upper left corner of Fig. 12-A) shows a noticeable increase in the days prior to X-class flaring (t=0). The variance for this Keylist (column 1, row 2) implies that most of the data is huddled around the mean across the entire time axis, but begin to disperse slightly just after flaring occurs. The skewness tends to hover around 0, but stays primarily in the positive region, which remains consistent with our interpretation of the variance. The kurtosis also shows that the distribution is nearly Gaussian most of the time. All of this means that for X-class flares, GWIL very typically increases for days prior to the large flare, and remains at a roughly constant value for at least 2 days afterward. However, note that the dip in the number of data points contributing to the statistical measures drops suddenly after the major flare. This feature is common to the X, M, and quiet Keylists, all of which contain flares, and remains unexplained.

The M-class flare Keylist (Fig. 12-A, right column) displays behavior quite different from that of the X-class flare Keylist. The mean and variance increase over the entire time interval, while the skewness suggests that the data tend to be on the weaker side of the average. The kurtosis implies that the distribution is sharply peaked at early time and flattens out as the AR progresses across the disk. This implies that there are a few outliers that play a significant role, but as more data points contribute, the variance becomes primarily due to moderate sized fluctuations. While the effect of the early outliers is dampened the variance continues to rise, suggesting that the distribution is broadening as time progresses. Therefore, as more points are added that seem to have little tendency to fall near the mean value, the mean still increases. The fact that skewness is positive nearly the entire time is puzzling, because it would seem that most of the points are falling to the right of the mean, which should cause the skewness to evolve toward larger negative values. We observe this near the beginning of the graph but the trend does not continue, which may be due to a flattening of the distribution at the same time.

The quiet (B- and C- class flare) Keylist (Fig 12-B, left column) displays the same characteristics as the M Keylist. This suggests that perhaps GWIL is insensitive to when the flare occurs, but may still be useful in characterizing whether or not an AR will flare at all. To test this, we look at the characteristics of GWIL in ARs that do not produce any flares.

The Dead-Silent Keylist (Fig. 12-B, right column) seems to display no overall tendencies. There is a general increase prior to the Keytime, but this is likely due to the increase in the number of points contributing to the statistical measures since there were only a handful of points early on. There is a peak in the variance roughly 20 hours after the Keytime that corresponds to an increase in the mean. Immediately after this peak, the kurtosis makes a similar jump. This suggests that a few of the data series began to have a large divergence from the norm. This could be the result of a flare-unassociated CME over a particular active region. If GWIL is sensitive to this type of CME, then we expect to see a large increase in the mean and variance of all the data series. If GWIL responds similarly to flare-unassociated CMEs as it does to X-class flares, we would expect it to remain roughly constant after the event. This would mean that an outlier would be present for some duration of time, causing the observed spike in the kurtosis.

The effective distance did not display very coherent results. The mean remained nearly constant except at the Keytime where it had a large spike in variance for X, M, and quiet flares. We include the SPE plots in the appendix for completeness.

IV. CONCLUSIONS

Automatic solar flare and coronal mass ejection forecasting is a crucial component of space weather. In this study, we have developed a software routine for automatically calculating the total magnetic flux of an active region, the distance between flux weighted centers of the bipolar regions, the primary netural line and its length, the gradient across the PNL, and the gradient weighted primary neutral line length. Each of these variables, other than the total flux, is a measure of either magnetic field complexity or nonpotential energy storage, which are both correlated with solar flares and CMEs. This code has been run on over 70,000 magnetograms containing 1075 active regions. Another program has

been written to produce superposed epoch plots given a Keylist. These plots will only be useful for a statistical size Keylist, as its primary purpose is to pick out weak pre- or post-flare signals. If strong signals were present in individual plots of these variables, they would have been detected and characterized in previous studies.

We have found that GWIL shows promise as an indicator for X-class flares. Flares of this strength are strongly correlated with the occurrence of CMEs. At this time, our analysis of the SPE plots remains primarily qualitative. Future work will include developing a quantitative measure for these plots. The drop in the number of data points contributing to the statistical measure immediately after flaring is an issue that remains to be resolved.

The number of quantities that we can calculate from line-of-sight magnetograms is limited. Many of the magnetic measures that show the most promise for flare/CME prediction can only be derived from vector magnetograms. Unfortunately, this type of data is sparse and typically not full-disk. This makes obtaining statistically significant results derived from vector magnetograms difficult. The Solar Dynamics Observatory (SDO) is set to launch later this year, which will contain the Helioseismic and Magnetic Imager (HMI). This instrument will take high resolution full-disk vector magnetic images every 90 seconds. As mentioned in the Data Analysis section, there are multiple researchers developing methods of automated image recognition software. Given this capability, we will soon be developing a C++ version of our code (including additional magnetic measures) to run in near real time using HMI data. The final output of the code will be a solar flare/CME forecast for each active region identified on the disk.

ACKNOWLEDGEMENTS

I would like to thank Todd Hoeksema for all the guidance, help, and opportunity he has given me. I'm also grateful for the answers, tips, edits, and general knowledge that I have gained from Phil Scherrer and Yang Liu. Special thanks to David Falconer for allowing me access to his unpublished data and results for comparison and his help with some of the very specific and technical questions I had about measuring the gradient weighted primary neutral line length. Additional thanks to Adriane Steinacker for practically re-learning a whole subject in order to help me understand my own research better and to Megan Shabram for editing this thesis at particularly odd hours of the night.

REFERENCES

Alissandrakis, C E. "On the Computation of Constant Alpha Force-free Magnetic Field." *Astronomy and Astrophysics*, 1981: 197-200.

Andrews, M D. "A Search for CMEs Associated with Big Flares." *Solar Physics* 218 (2003): 261-279.

Barnes, G, and K D Leka. "Evaluating the Performance of Solar Flare Forecasting Methods." *Astrophysical Journal* 688 (2008): 107-110.

Bokenkamp, N. *Statistical Relationships Between Solar Active Region Photospheric Magnetic Properties and Flare Events.* Senior Thesis, Stanford University, 2007.

Chumak, O V, and Z N Chumak. "A Stochastic Method of Describing the Evolution of Solar Active Regions." *Kinematika i Fizika Nebesnykh Tel* 3 (1987): 7-13.

Chumak, O, H Zhang, and J Gou. "Integral properties of the Magnetic Fields of Solar Active Regions Under Quiet and Flare Activity Conditions." *Astronomical and Astrophysical Transactions* 23, no. 6 (2004): 525-531.

Falconer, D A, and G A Moore. "A Measure from Line-of-Sight Magnetograms for Prediction of Coronal Mass Ejections." *Journal of Geophysical Research* 108 (2003): SSH 11-1 SSH 11-7.

Falconer, D A, R L Moore, and G A Gary. "Correlation of the Coronal Mass Ejection Productivity of Solar Active Regions with Measures of Their Global Nonpotentiality from Vector Magnetograms: Baseline Results." *Astrophysical Journal* 569 (2001): 1016-1025.

Feynman, J., and A. J. Hundhausen. "Coronal Mass Ejections and Major Solar Flares: The Great Active Center of March 1989." *Journal of Geophysical Research*, 1994: 8451-8464.

Forbes, T G, et al. "CME Theory and Models." *Space Science Reviews*, 2006: 251-302.

Gopalswamy, Nat, Alejandro Lara, Seiji Yashiro, Mike L Kaiser, and Howard A Russell. "Predicting the 1-AU Arrival Times of Coronal Mass Ejections." *Journal of Geophysical Research* 106 (2001): 207-229.

Guo, J, and H Zhang. "A Quantitative Study on Magnetic Configuration for Active Regions." *Solar Physics*, 2006: 25-43.

Gurman, Joseph B. *Solar Monitor.* March 22, 2000. http://www.solarmonitor.org/full_disk.php?date=20000322&type=smdi_maglc (accessed April 7, 2009).

Harrison, R A. "Coronal Magnetic Storms: a New Perspective on Flares and the `Solar Flare Myth' Debate." *Solar Physics*, 1996: 441-444.

Hathaway, David H. *NASA Marshall Space Flight Center.* January 18, 2007. http://solarscience.msfc.nasa.gov/CMEs.shtml (accessed April 1, 2009).

Hathaway, David. *NASA Marshall Space Flight Center.* March 4, 2009. http://solarscience.msfc.nasa.gov/SunspotCycle.shtml (accessed April 1, 2009).

Haubold, Hans, and A M Mathai. "Sun." *Encyclopedia of Planetary Sciences*, 1997: 786-794.

Hudson, Hugh S. "The Unpredictability of the Most Energetic Solar Events." *Astrophysical Journal* 663 (2007): 45-48.

Kahler, S W. "Solar Flares and Coronal Mass Ejections." *Astronomy and Astrophysics*, 1992: 113-141.

Kallenrode, May-Britt. *Space Physics: An Introduction to Plasmas and Particles in the heliosphere and Magnetospheres.* New York: Springer-Verlag Berlin Heidelberg, 1998.
Leka, K D, and G Barnes. "Photospheric Magnetic Field Properties of Flaring Versus Flare-Quiet Acive Regions. IV. A Statistically Significant Sample." *Astrophysical Journal* 656 (2006): 1173-1186.
Leka, K D, and G Barnes. "Photospheric Magnetic Field properties of Flaring Versus Flare-quiet Active regions. I. Date, General Approach, and Sample Results." *Astrophysical Journal*, October 2003: 1277-1295.
Linker, Jon A, Zoran Mikic, Roberto Lionello, Pete Riley, Tahar Amari, and Dusan Odstrcil. "Flux Cancellation and Coronal Mass Ejections." *Physics of Plasmas* 10, no. 5 (2003): 1971-1978.
Liu, Y, A A Norton, and P H Scherrer. "A Note on Saturation Seen in the MDI/SOHO Magnetograms." *Solar Physics* 241, no. 1 (2007): 185-193.
Low, B C. "Coronal Mass Ejections, Magnetic Flux Ropes, and Solar Magnetism." *Journal of Geophysical Research* 106, no. A11 (2001): 25141-25164.
McIntosh, Patrick S. "The Classification of Sunspot Groups." *Solar Physics* 125 (1990): 251-267.
Meriam. "The Aurora Borealis.; The Brilliant Display on Sunday Night." *New York Times*, August 30, 1859: 1.
Press, William H, Saul A Teukolsky, William T Vetterling, and Brian P Flannery. *Numerical recipes 3rd Edition.* Cambridge: Cambridge University Press, 2007.
Rohde, Robert A. *Global Warming Art project.* April 17, 2008. http://www.globalwarmingart.com/wiki/Image:Solar_Cycle_Variations_png (accessed April 1, 2009).
Scherrer, P H, et al. "The Solar Oscillations Investigation - Michelson Doppler Imager." *Solar Physics* 162, no. 1-2 (1995): 129-188.
Schrijver, Carolus J. "Driving Major Solar Flares and Eruptions: A Review." *Advances in Space Research*, 2009: 739-755.
Song, H, V Yurchyshyn, G Yang, C Tan, W Chen, and H Wang. "The Automatic Predictability of Super Geomagnetic Storms From Halo CMEs Associated with Large Solar Flares." *Solar Physics*, 2006: 141-165.
Srivastava, Nandita, and P Venkatakrishnan. "Solar and Interplanetary Sources of major Geomagnetic Storms During 1996-2002." *Journal of Geophysical Research* 109, no. A10 (2004).
Sturrock, P A. "Maximum Energy of Semi-Infinite Magnetic Field Configurations." *Astrophysical Journal* 380 (1991): 655-659.
Wang, Y, and J Zhang. "A Comparative Study Between Eruptive X-Class Flares Associated with Coronal Mass Ejections and Confined X-Class Flares." *Astrophysical Journal* 665 (2007): 1428.
Yashiro, S, N Gopalswamy, S Akiyama, G Michalek, and R A Howard. "Visibility of Coronal Mass Ejections as a Function of Flare Location and Intensity." *Space Physics*, 2005: 12.
Zirker, Zack B. *Journey from the Center of the Sun.* Princeton: Princeton University Press, 2002.

GLOSSARY

Active Region (AR): An area on the solar surface (photosphere) of exceptional magnetic activity. They exist below, and are the cause of, sunspots.

Alvén wave: Magnetohydrodynamic (MHD) transverse wave that propagates along the magnetic field lines (like a plucked string). Magnetic tension acts as the restoring force. Magnetosonic waves are MHD longitudinal waves.

Central Meridian: The longitudinal center of a disk/sphere.

Compact/Confined Flares: These are flares that are unassociated with Coronal Mass Ejections (CME). They are caused by tight, low flux ropes with very strong magnetic fields (several hundred Gauss). They primarily emit hard x-rays. CMEs that exist without a flare tend to have low velocity but a large acceleration.

Eruptive/Gradual Flares: These are flares that are associated with CMEs. Eruptive flares emit hard and soft x-rays and visible light. The associated CMEs tend to have very high velocity.

Filament: A large dark feature on the solar disk caused by a flux rope.

Flux ropes: Loops of magnetic field that extends from the solar convective zone to the corona. The loops contain plasma that is pumped up one end of the loop and out of the other.

Lagrange Points: Any 3-body gravitational system has a few points where gravity and centrifugal force balance in the rotating reference frame. These are known as Lagrangian points. The L1 point is directly between the two largest bodies (e.g. the earth and sun).

Magnetic helicity: Degree to which a magnetic field twists around itself. There are many such parameters to describe how an electromagnetic field can become twisted and sheared.

Magnetic reconnection: Magnetic field lines existing in a nonpotential configuration come into contact with one another and reconfigure into a lower energy state.

Neutral line and Primary Neutral (Inversion) Line: Boundary between flux regions of opposite polarity. The Primary Neutral Line (PNL) is the boundary between the major bipolar region of an active region

Nonpotentiality/Nonpotential energy: Energy stored in a magnetic field that is in excess of the lowest energy configuration (i.e. potential force-free field).

Prominence: A large bright feature extending from the solar limb (edge of disk) caused by a flux rope.

White light: Entire visible portion of the electromagnetic spectrum.

APPENDIX

BASIC STRUCTURE OF THE SUN

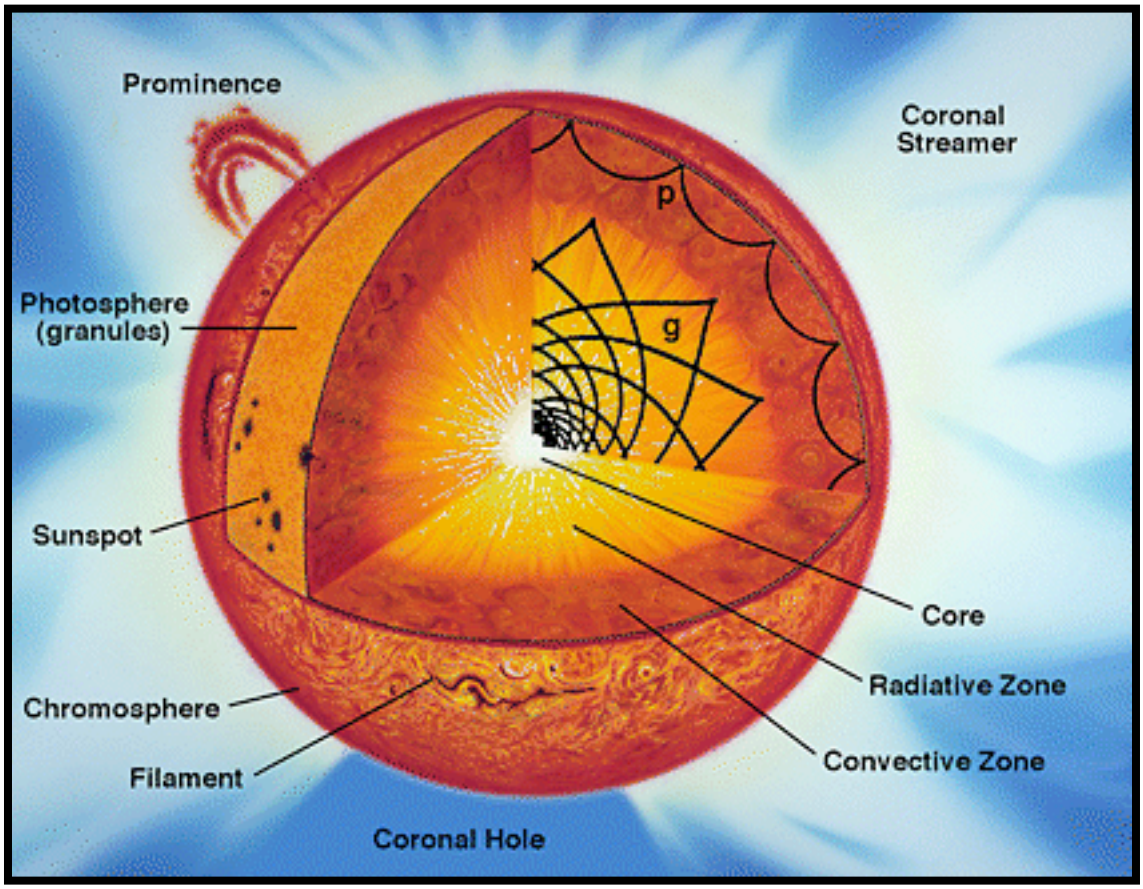

***Figure 13*: Diagram of solar structure with labels. (Haubold and Mathai 1997)**

The core of the sun extends to roughly $0.2R_{\odot}$[14] and a temperature of 15.7×10^6 Kelvin. Here, the fusion of hydrogen into helium powers the sun and balances its gravitational pressure. The radiative zone extends from the core to about $0.7\ R_{\odot}$ and consists of a highly ionized plasma where the density and pressure is so high photons must diffuse outward. It may take several million years for any individual photon to "random walk" its way out of the entire sun. This causes large temperature gradients in the solar interior, which in turn drive convective currents. The convective zone extends from the radiative zone to just less than $1R_{\odot}$. The cyclic convective currents are an alternate method of transferring the large thermal

[14] $R_{\odot} = 6.96 \times 10^8$ meters

energy to the solar surface where it can finally be radiated. The plasma at the surface cools, causing it to drop back into the solar interior where it can collect more heat from the radiative zone. The outermost convection zone is full of turbulence, which generates small-scale dynamos that cause the granulation of the solar surface. The photosphere (solar surface) has a temperature of about 6000 Kelvin and is only about $0.002R_{\odot}$ and is the location where white-light photons escape the sun. Once they leave, it only takes about 8 minutes for them to reach 1 Astronomical Unit (AU) i.e. the distance from the sun to the earth. The chromosphere is a $0.02R_{\odot}$ thick layer that lies on top of the photosphere with a considerably higher temperature that reaches nearly 100,000 Kelvin. The corona's outer boundary is somewhat ill defined as it blends with the solar wind that extends through the solar system. The low corona has a temperature of several million Kelvin. This enormous temperature has yet to be explained by theory.

WHY ARE SUNSPOTS DARK?

Active regions are known to lie beneath sunspots. The magnetic field of the AR provides pressure to the surrounding plasma that can alleviate the pressure needed to keep the material in equilibrium with the material around it. This alleviated pressure allows the plasma to cool. The Stefan-Boltzmann law for a blackbody

$$E \propto \sigma T^4 \tag{4}$$

states that the emitted energy is proportional to the temperature to the fourth power. Therefore, solar material that has a lower temperature will emit less light causing the region to appear darker than its surroundings. However, if a sunspot were to be hung in the sky by itself, it would appear as a bright orange object.

EFFECTIVE DISTANCE SUPERPOSED EPOCH PLOTS

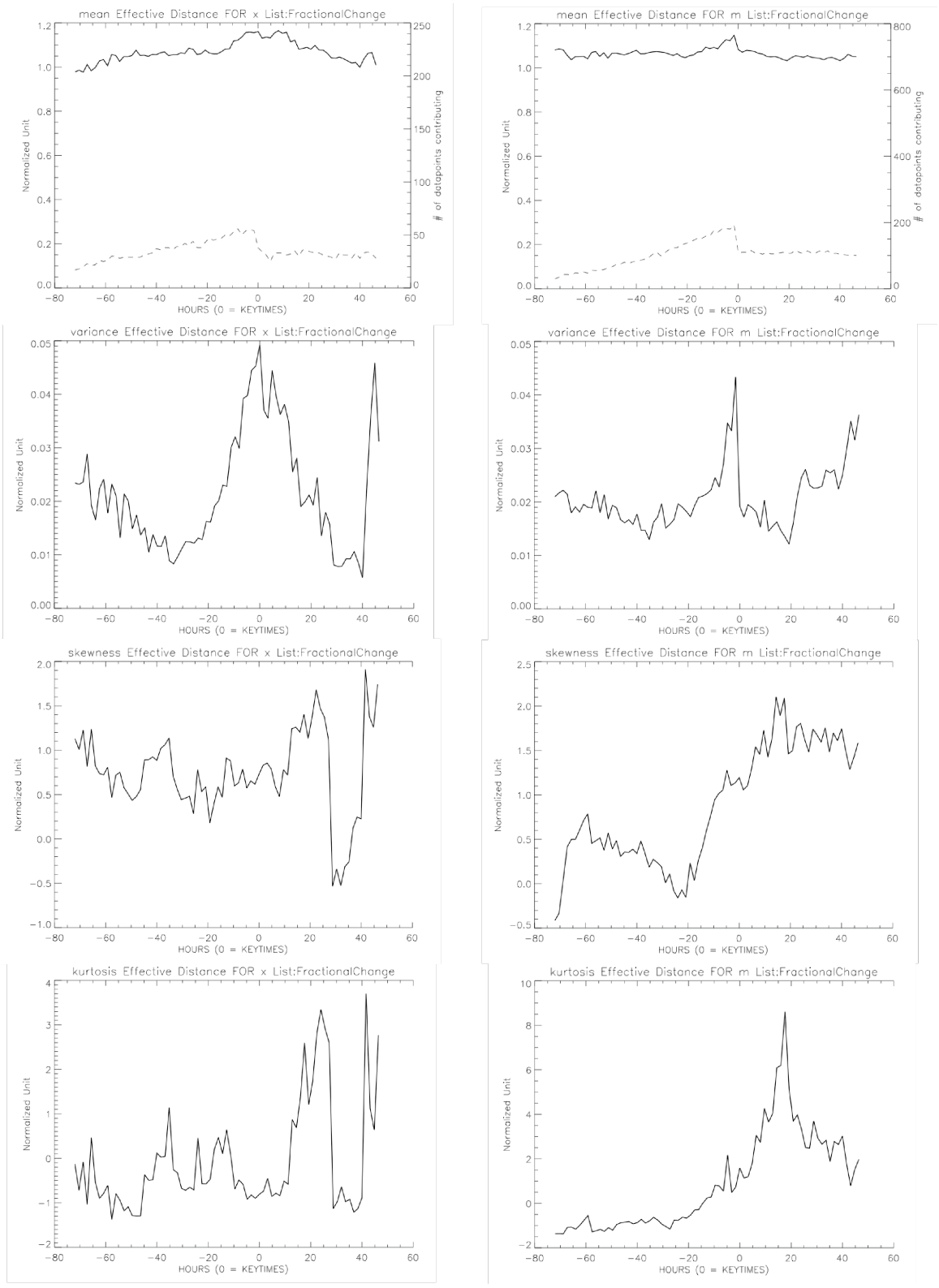

***Figure 14-A*: Same as Figure 12-A, but of the Effective Distance.**

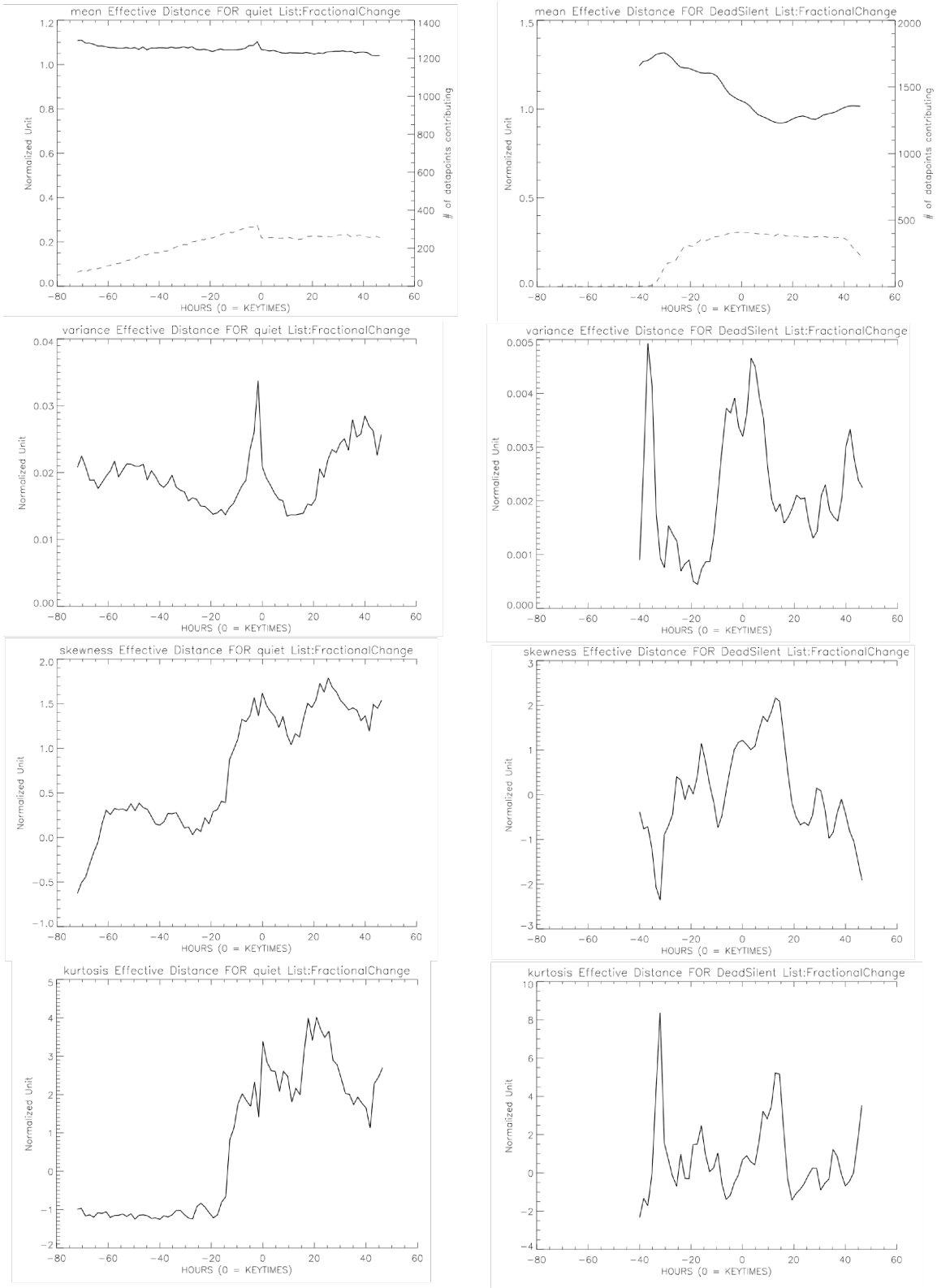

Figure 13-B: **Same as Figure 12-B, but of Effective Distance.**